

*accepted for publication in The Astrophysical Journal Supplements*

## **Axisymmetric Three-Integral Models for Galaxies**

N. Cretton, P. Tim de Zeeuw,  
Sterrewacht Leiden, Postbus 9513, 2300 RA Leiden, The Netherlands

Roeland P. van der Marel,  
Space Telescope Science Institute, 3700 San Martin Drive, Baltimore, MD 21218

Hans-Walter Rix<sup>1,2</sup>  
Steward Observatory, University of Arizona, Tucson, AZ 85721

---

<sup>1</sup>Alfred P. Sloan Fellow

<sup>2</sup>present address: Max-Planck-Institut für Astronomie, Königstuhl 17, Heidelberg, Germany

## ABSTRACT

We describe an improved, practical method for constructing galaxy models that match an arbitrary set of observational constraints, without prior assumptions about the phase-space distribution function (DF). Our method is an extension of Schwarzschild’s orbit superposition technique. As in Schwarzschild’s original implementation, we compute a representative library of orbits in a given potential. We then project each orbit onto the space of observables, consisting of position on the sky and line-of-sight velocity, while properly taking into account seeing convolution and pixel binning. We find the combination of orbits that produces a dynamical model that best fits the observed photometry and kinematics of the galaxy. A new element of this work is the ability to predict and match to the data the full line-of-sight velocity profile shapes. A dark component (such as a black hole and/or a dark halo) can easily be included in the models.

In an earlier paper (Rix et al.) we described the basic principles, and implemented them for the simplest case of spherical geometry. Here we focus on the axisymmetric case. We first show how to build galaxy models from individual orbits. This provides a method to build models with fully general DFs, without the need for analytic integrals of motion. We then discuss a set of alternative building blocks, the two-integral and the isotropic components, for which the observable properties can be computed analytically. Models built entirely from the two-integral components yield DFs of the form  $f(E, L_z)$ , which depend only on the energy  $E$  and angular momentum  $L_z$ . This provides a new method to construct such models. The smoothness of the two-integral and isotropic components also makes them convenient to use in conjunction with the regular orbits.

We have tested our method, by using it to reconstruct the properties of a two-integral model built with independent software. The test model is reproduced satisfactorily, either with the regular orbits, or with the two-integral components. This paper mainly deals with the technical aspects of the method, while applications to the galaxies M32 and NGC 4342 are described elsewhere (van der Marel et al., Cretton & van den Bosch).

*Subject headings:* black hole physics — galaxies: elliptical and lenticular, cD — galaxies: kinematics and dynamics — galaxies: structure.

## 1. Introduction

In order to understand the structure and dynamics of a galaxy, one needs to measure the total gravitational potential as well as the phase-space distribution function (DF) of the constituent stars. The DF specifies the distribution of the stars over position and velocity, and hence provides a full description of the galaxy. For a particular galaxy, one needs to explore which combinations of potential and DF are consistent with the available observations (surface brightness and kinematics). Several methods have been devised to tackle this problem.

The direct calculation of the DF generally requires analytic knowledge of the integrals of motion, and has been restricted in the past to a number of special cases: (i) spherical or other integrable potentials (e.g., Dejonghe 1984, 1986; Bishop 1987; Dejonghe & de Zeeuw 1988; Gerhard 1991; Hunter & de Zeeuw 1992); (ii) nearly integrable systems where perturbation theory can be applied (Saaf 1968; Dehnen & Gerhard 1993); or (iii) the subset of axisymmetric models in which the DF is *assumed* to depend only on  $E$  and  $L_z$  (Hunter & Qian 1993; Dehnen & Gerhard 1994; Kuijken 1995; Qian et al. 1995, hereafter Q95; Magorrian 1995; Merritt 1996b, hereafter M96b). Numerical calculations of orbits in axisymmetric potentials have shown that most of the orbits admit a third integral, which in general is not known analytically (e.g., Ollongren 1962). There is no a priori physical reason to expect the DF to depend only on the two classical integrals, and in fact, there are indications for both elliptical galaxies (Binney, Davies & Illingworth 1990) and halos of spirals (Morrison, Flynn & Freeman 1990) that the DF must depend also on the third integral. For the solar neighborhood it has been known for a long time that there must be such a dependence (e.g., Binney & Merrifield 1998).

Schwarzschild (1979, 1982) devised an elegant method to circumvent our ignorance of analytic integrals of motion and to build numerically self-consistent equilibrium models of galaxies. Richstone (1980, 1984) used this technique to construct axisymmetric scale-free models. It was applied to a variety of models (spherical, axisymmetric and triaxial) by Richstone and collaborators (see e.g., Richstone & Tremaine 1984, 1985; Levison & Richstone 1985, 1987; Katz & Richstone 1985). Pfenniger (1984) used Schwarzschild’s method to build two-dimensional models of barred galaxies and Merritt & Fridman (1996) and Merritt (1996a) used it to build a number of triaxial models with cusps. Zhao (1996b) modeled the Galactic bar using similar techniques. Schwarzschild’s original experiment reproduced self-consistently a triaxial mass distribution, but as shown by Pfenniger (1984), one can easily include kinematic constraints in the models. Levison & Richstone (1985) modeled the observed mean line-of-sight velocities  $V$  and velocity dispersions  $\sigma$  to estimate the amount of counter-rotation in some well-observed galaxies.

Recent advances in detector technology have made it possible to measure full line-of-sight velocity profile (VP) shapes, instead of only the first two moments  $V$  and  $\sigma$  (e.g., Franx & Illingworth 1988; Rix & White 1992; van der Marel & Franx 1993, hereafter vdMF; Kuijken & Merrifield 1993). This provides further constraints on the dynamical structure of galaxies. Rix et al. (1997, hereafter R97) took advantage of this development, and extended Schwarzschild’s scheme to model VP shapes. They applied it to spherical models for the E0 galaxy NGC 2434, and showed that the observations imply the presence of a dark halo. Here we consider axisymmetric models and show how to use the extended Schwarzschild method to construct fully general three-integral

models that can match any set of kinematic constraints. Independent implementations of the software were written by N.C. and R.v.d.M. A summary of this development is given by de Zeeuw (1997). In an earlier paper (van der Marel et al. 1998, hereafter vdM98; see also van der Marel et al. 1997) we applied this modeling technique to the compact E3 elliptical M32, for which previous modeling had suggested the presence of a central massive black hole (BH) (e.g., Q95; Dehnen 1995). Cretton & van den Bosch (1999) describe an application to the edge-on S0 galaxy NGC 4342. Other groups are in the process of developing similar techniques to the one described here (e.g., Richstone et al. 1997; see also: Emsellem, Dejonghe & Bacon 1999; Matthias & Gerhard 1999).

This paper is organized as follows. In Section 2 we describe step by step how to construct the models (see Figure 1). We first discuss the mass models that we consider (Section 2.1). We describe how we choose a grid in integral space that yields a representative library of orbits (Section 2.2), how these orbits are calculated numerically (Section 2.3), how their properties are stored on a number of grids (Section 2.4), and how we model all aspects of the data taking and analysis, such as seeing convolution, pixel binning, and extraction of VPs (Section 2.5). We then present the method that we employ to determine the non-negative weight of each orbit (i.e., the number of stars traveling on each orbit), such that the global superposition of orbits produces a consistent model that best fits the observations (Section 2.6). Lastly, we discuss how we include optional smoothness constraints in the models (Section 2.7). In Section 3 we describe a set of alternative building blocks, the two-integral and isotropic components, for which the observable properties can be computed analytically. The smoothness of these components makes them a convenient tool to use in conjunction with the regular orbits described in Section 2. Models can also be built entirely of these components, to obtain models with DFs of the form  $f(E, L_z)$  or  $f(E)$ . In Section 4 we describe the tests that we have performed to establish the accuracy of our method. We present our conclusions in Section 5.

## 2. Construction of Dynamical Models

### 2.1. Mass Model

We study dynamical models in which all relevant quantities are axisymmetric, and symmetric with respect to the equatorial plane  $z = 0$ . It is sufficient to have the total gravitational potential,  $\Phi \equiv \Phi_\star + \Phi_{\text{dark}}$ , and the forces,  $\vec{\nabla}\Phi$  available and tabulated on a grid, such that their values at any point can be recovered through interpolation. This is important, because the structure of real galaxies can be very complicated, and is not always well described in terms of analytical functions.

While the method works for arbitrary radial density profiles, it proves convenient for the purpose of presenting and testing our technique to consider models in which the mass density of the luminous material,  $\rho_\star$ , does have an analytical form:

$$\rho_\star(R, z) = \rho(s) = \rho_0 \left[ \frac{s}{b} \right]^\alpha \left( 1 + \left[ \frac{s}{b} \right]^\gamma \right)^\beta \left( 1 + \left[ \frac{s}{c} \right]^\epsilon \right)^\delta, \quad (1)$$

where  $s$  is defined as  $s^2 = R^2 + (z/q)^2$ . This is an axisymmetric generalization of the spherical

models studied previously by, e.g., Dehnen (1993), Tremaine et al. (1994) and Zhao (1996a), and includes the  $(\alpha, \beta)$  models of Q95 as a limiting case. The model has a constant axial ratio  $q$  that does not vary with radius. The parameters  $b$  and  $c$  are characteristic lengths. At small radii ( $r \ll b$ ) the density has a central cusp with logarithmic slope  $\alpha$  (when  $\alpha < 0$ ). At intermediate radii ( $b \ll r \ll c$ ) the density falls off as  $\rho_\star \propto r^{\alpha+\gamma\beta}$ , while at large radii ( $r \gg c$ )  $\rho_\star \propto r^{\alpha+\gamma\beta+\epsilon\delta}$ . When viewed at an inclination angle  $i$ , the isophotes are ellipses of axial ratio  $q' = (\cos^2 i + q^2 \sin^2 i)^{1/2}$ . The luminosity density is  $j = \rho_\star/\Upsilon$ , where  $\Upsilon$  is the average mass-to-light-ratio of the luminous material, which we assume to be constant.

For these models, the gravitational potential and the associated radial and vertical forces can all be obtained from one-dimensional (usually numerical) integrals (cf. eqs. [2.10]–[2.12] of Q95). We calculate the potential and forces in this way and tabulate them on a fine polar  $(r, \theta)$  grid, with logarithmic sampling in radius and linear sampling in the angle. These tabulated values are used for the subsequent orbit calculations. It is straightforward to add the contributions from a dark component to the potential and the forces, as required for models with, e.g., a BH or a dark halo. In the case of a BH these contributions need not be tabulated, because they are known analytically.

For density distributions that are not stratified on similar concentric spheroids one must use more general techniques to calculate the gravitational potential and the associated forces. One possibility to determine these, while at the same time fitting a complicated surface brightness distribution, is to use a Multi-Gaussian Expansion (Emsellem et al. 1994). We do this in our modeling of the S0 galaxy NGC 4342 (Cretton & van den Bosch 1999). Another possibility is to obtain  $\rho_\star$  through non-parametric deprojection of an observed surface brightness distribution (e.g., Dehnen 1995), and calculate the potential from a multipole or other expansion (e.g., Hernquist & Ostriker 1992; Zhao 1996a).

## 2.2. Choice of Orbits

The results obtained with our modeling technique should not depend on the details of the orbit library. To achieve this, the library must represent the full variety of orbits in the given potential. In this section we describe how we have chosen to select orbits in order to fulfill this requirement.

In axisymmetric models, all orbits conserve at least two isolating integrals of motion: the energy  $E$  and the vertical component of the angular momentum  $L_z$ . Numerical studies have shown that many orbits conserve an additional third isolating integral  $I_3$ , which is usually not known analytically (see e.g., Ollongren 1962; Innanen & Papp 1977; Richstone 1982; Dehnen & Gerhard 1993). These *regular* orbits are specified completely by the integrals of motion, and can be labeled by the values of  $E$ ,  $L_z$  and  $I_3$ .

For each energy  $E$ , there is one circular orbit in the equatorial plane, which has radius  $R_c$  and velocity  $V_c^2 = R_c(\partial\Phi/\partial R)_{(R_c,0)}$ . The angular momentum of this orbit,  $R_c V_c$ , is the maximum angular momentum at the given energy:  $L_{\max}(E)$ . We sample the energies in the model by

adopting a logarithmic grid in  $R_c$ . Each  $R_c$  defines an energy  $E$  through the implicit relation  $E = \Phi(R_c, 0) + \frac{1}{2}V_c^2$ . The orbits in the model have  $R_c \in [0, \infty)$ . However, it is sufficient to adopt a grid of  $N_E$  values that covers only a finite range,  $R_{c,\min}$  to  $R_{c,\max}$ , chosen so as to contain all but a negligible fraction of the total mass of the system. At each energy we sample the range of possible  $L_z$  values by adopting a grid in the quantity  $\eta \equiv L_z/L_{\max}(E)$  ( $\eta \in [-1, 1]$ ). Orbits with both  $L_z > 0$  and  $L_z < 0$  are included in the library, but the  $L_z < 0$  orbits need not be calculated; they are obtained from the  $L_z > 0$  orbits by reversing the velocity vector at each point along the orbit. We have calculated orbits for  $N_\eta$  values of  $\eta$ , spaced linearly between  $\epsilon_1$  and  $1 - \epsilon_1$ , where  $\epsilon_1$  is a small number. For numerical reasons, the special values  $\eta = 0$  (radial orbits) and  $\eta = 1$  (the circular orbit in the equatorial plane) are presumed to be represented by their closest neighbors on the grid, but are not included explicitly.

In an axisymmetric potential the orbit reduces to a two-dimensional motion in the meridional  $(R, z)$  plane in an effective gravitational potential  $\Phi_{\text{eff}} = \Phi + \frac{1}{2}L_z^2/R^2$  (e.g., Binney & Tremaine 1987, hereafter BT). For fixed  $(E, L_z)$ , the position of a star is restricted to the region bounded by the ‘zero-velocity curve’ (ZVC), defined as the curve of values  $(R, z)$  that satisfy the equation  $E = \Phi_{\text{eff}}$ , and hence  $v_R = v_z = 0$ . Figure 2 illustrates ZVCs in the meridional plane. A regular orbit admits a third isolating integral,  $I_3$ , that restricts its motion to a sub-region of the full region of phase-space accessible at the given  $(E, L_z)$ . This is illustrated in Figure 3, which shows a regular orbit viewed in the meridional plane. In our method we have chosen a numerical representation of  $I_3$  that can be used to label the orbit. Every orbit with  $L_z \neq 0$  touches the ZVC (Ollongren 1962). As suggested by Levison & Richstone (1985), we take the  $R$  coordinate of the ‘turning point’ on the ZVC (i.e., the intersection of the orbit with the ZVC), denoted by  $R_{\text{zvc}}$ , as the third parameter to specify the orbit. At every  $(E, L_z)$  there is exactly one orbit that touches the ZVC at only one value,  $R_{\text{thin}}$ , of  $R$ : the so-called ‘thin tube’ orbit (see Figure 3). All other regular orbits touch the ZVC for at least two values of  $R_{\text{zvc}}$ , one smaller than  $R_{\text{thin}}$  and one larger than  $R_{\text{thin}}$ . To sample the orbits at a given  $(E, L_z)$ , we calculate trajectories that are started with  $v_R = v_z = 0$  from the ZVC, at a given radius  $R_{\text{zvc}}$  (this radius determines  $v_\phi$  according to  $v_\phi = L_z/R$ ). Not every orbit launched in this way necessarily admits a third integral, since irregular orbits also touch the ZVC. Our orbit library therefore includes both regular and irregular orbits, and, as we shall see in Section 2.3, we have found it unnecessary to distinguish between them in all our tests and applications to date. To reduce redundancy in the library it is sufficient to consider only orbits with  $R_{\text{zvc}} \in [R_{\text{thin}}, R_{\text{max}}]$ , where  $R_{\text{max}}$  is the radius at which the ZVC intersects the plane  $z = 0$ .

For the orbit library we have chosen to use  $N_{I_3}$  values of  $R_{\text{zvc}}$ . Each point  $(R_{\text{zvc}}, z_{\text{zvc}})$  on the ZVC is determined with the help of an angle  $w$ , which is sampled linearly between 0 and  $w_{\text{thin}}$  (see Figure 3). For numerical reasons, the special values  $R_{\text{zvc}} = R_{\text{thin}}$  (thin tube orbit) and  $R_{\text{zvc}} = R_{\text{max}}$  (equatorial orbit) are presumed to be represented by their respective closest neighbor on the grid, but are not included explicitly. Finding the starting point for the periodic orbit,  $R_{\text{thin}}$ , is straightforward (see e.g. Pfenniger & Friedli, 1993).

It is sufficient to calculate only orbits that are started from the ZVC with  $z > 0$ . Orbits started with  $z < 0$  are obtained from those started with  $z > 0$  by reversing the sign of  $z$  and  $v_z$  at each point along the orbit. Most orbits are themselves symmetric with respect to the equatorial plane (see e.g., Figure 3), so that this operation is redundant. However, this is not true for, e.g.,

the orbits parented by the 1/1 resonance between the  $R$  and  $z$ -motion (see Figure 11 below, or Figure 8 of Richstone 1982). Since we are only interested in constructing models that are symmetric about the equatorial plane, we do not view the orbits started with  $z > 0$  and  $z < 0$  from the ZVC as separate building blocks, but instead we consider only their sum.

The grid in  $(R_c, \eta, R_{zvc})$  completely specifies the orbit library. Appropriate choices for the parameters that characterize this grid are discussed in Section 4.

### 2.3. Orbit Calculation

For each  $(R_c, \eta, R_{zvc})$  we calculate a trajectory, started from the ZVC as described in Section 2.2. We have used several standard integration algorithms, including the Bulirsch-Stoer integrator (Press et al. 1992) and the Runge-Kutta-Fehlberg algorithm (Fehlberg 1968). We have experimented with both and found equivalent results. The former algorithm was used in vdM98. Here we use the Runge-Kutta-Fehlberg algorithm.

The results of the orbit calculations were used to approximate the ‘orbital phase-space density’ for each trajectory. Each phase-point along a calculated orbit was assigned a weight equal to the time step at that point, divided by the total integration time.

This procedure results in density distributions in phase-space,  $DF_{\text{traj}}$  and its corresponding spatial density  $\rho_{\text{traj}}$ . Orbits were calculated in the meridional plane, but all six phase-space coordinates are needed. The azimuthal velocity  $v_\phi = L_z/R$  is completely specified. However, for projection onto the sky, the azimuthal angle  $\phi \in [0, 2\pi]$  is also required. The distribution of stars over  $\phi$  is homogeneous, because of the assumed symmetry. The weight at each time step was therefore divided into a number of equal ‘sub-weights’, and each was assigned a random  $\phi$ . Furthermore, each sub-weight was divided in two, and one of the two parts was assigned phase-coordinates with  $(z, v_z)$  multiplied by  $-1$ . This corrects for the fact that only orbits started with  $z > 0$  from the ZVC were calculated (cf. Section 2.2). The trajectories should be integrated long enough so that the orbital phase-space densities no longer change significantly with time. Pfenniger (1984) proposed to check directly for the convergence of the orbital mass distribution. However, this may take a very long time, especially for orbits that are unusually close to a high-order resonance, for orbits at very large radii or at very small radii close to a BH, and for irregular orbits (see also Merritt & Fridman 1996). We have used a cruder approach, in which we calculated each orbit for a fixed number ( $\sim 200$ ) of characteristic orbital periods. We found this to be sufficient for our purpose; longer integrations yield final models that are not significantly different. This is because the ‘noise’ in our modeling is dominated by the representation of phase space through a coarse discrete grid.

Orbits can have sharp edges in both the spatial and velocity dimensions. We found that a simple scheme to obtain smoother densities yielded slightly more accurate results for the final orbit superposition. To take into account the fact that each energy  $E$  in the orbit catalog represents all energies in some bin  $[E_1, E_2]$  around it (defined by the choice of energy grid), a random energy  $\bar{E}$  was drawn from the range  $[E_1, E_2]$  for each normalized time step. The

corresponding phase-coordinates  $(\vec{r}, \vec{v})$  were then translated to the energy  $\tilde{E}$ , by replacing them by  $([\tilde{R}_c/R_c]\vec{r}, [\tilde{V}_c/V_c]\vec{v})$ , where  $R_c$ ,  $\tilde{R}_c$  and  $V_c$ ,  $\tilde{V}_c$  are the radii and circular velocities of the circular orbits at the energies  $E$  and  $\tilde{E}$ , respectively. This “dithering” approach is only approximately correct (it assumes that the potential is locally scale-free), but was found to work well in practice.

## 2.4. Storing the Orbital Properties

For each orbit we store both the intrinsic properties and the projected properties. The intrinsic properties are necessary to test for consistency of the final model. We store  $\rho_{\text{traj}}$  on an  $(r, \theta)$  grid in the meridional plane, logarithmic in  $r$  and linear in  $\theta \in [0, \frac{\pi}{2}]$ . Angles  $\theta > \frac{\pi}{2}$  need not be stored separately, because of symmetry with respect to the equatorial plane. We also store the lowest-order velocity moments of each orbit  $(\rho_{\text{traj}}\langle v_i \rangle, \rho_{\text{traj}}\langle v_i v_j \rangle, i, j = r, \theta, \phi)$  on the same grid, so as to be able to study the intrinsic dynamical structure of the final model.

The projected properties are necessary for comparison to observable quantities, such as the projected surface brightness and line-of-sight VP shapes. Only three coordinates of phase-space are available for comparison with observations: the projected positions  $x', y'$  (which we choose to be aligned with the photometric major and minor axis), and the line-of-sight velocity,  $v_{\text{los}} (\equiv v_{z'})$ . Given an inclination angle  $i$  of the galaxy ( $i = 90^\circ$  means edge-on), these are related to the usual cylindrical coordinates  $(R, z, \phi)$  in the following way:

$$\begin{aligned} x' &= R \sin \phi, \\ y' &= -R \cos i \cos \phi + z \sin i, \\ v_{\text{los}} &= (v_R \cos \phi - v_\phi \sin \phi) \sin i + v_z \cos i. \end{aligned} \tag{2}$$

To have the projected properties of the orbits accessible, we store their phase-space densities both on an  $(r', \theta')$  grid on the projected plane of the sky (with similar properties as the intrinsic  $(r, \theta)$  grid), and on a Cartesian  $(x', y', v_{\text{los}})$  data cube (see Section 2.5). The former is used to reconstruct the projected surface density of the model. The latter is used to model observed kinematical quantities. The spatial grid size  $(\Delta x, \Delta y)$  of the  $(x', y', v_{\text{los}})$  cube is chosen to provide 2–5 times higher spatial resolution than the pixel size of the available kinematical observations. If observations with very different resolution are available for a galaxy (e.g., very high spatial resolution HST data in the central arcsec, and lower-resolution ground-based data out to an effective radius), it is best to store the data on two or more cubes with different spatial grid sizes and extents. During the orbit calculations we then store the phase-space densities simultaneously on all  $(x', y', v_{\text{los}})$  cubes. Only the  $x' \geq 0$  half of each cube needs to be stored, because each orbit has the same weight at  $(x', y', v_{\text{los}})$  as at  $(-x', -y', -v_{\text{los}})$ . The size  $\Delta v$  of the velocity bins on the  $(x', y', v_{\text{los}})$  cube(s) must be chosen to provide a proper sampling of the observed VPs. In practice we use  $\sim 50$ – $100$  bins between  $(-N_\sigma \sigma_{\text{max}}, N_\sigma \sigma_{\text{max}})$ , where  $\sigma_{\text{max}}$  is the largest observed dispersion, and  $N_\sigma = 4$ – $8$ .



## 2.5. Modeling Observed Kinematical Quantities

Point-spread-function (PSF) convolution is essential when comparing model quantities with observed kinematical quantities in the central regions of galaxies. Seeing convolution correlates information in the two spatial dimensions  $x', y'$ , but not in  $v_{\text{los}}$ :

$$F_{\text{conv}}(x'_0, y'_0, v_{\text{los}}) = F \otimes \text{PSF} = \iint F(x', y', v_{\text{los}}) \text{PSF}(x' - x'_0, y' - y'_0) dx' dy', \quad (3)$$

where  $F$  is the function to convolve, PSF is the point-spread function, and  $F_{\text{conv}}$  is the result of the convolution of  $F$  with the PSF. The final model is a linear superposition of the orbits, so the  $(x', y', v_{\text{los}})$  cubes for each orbit may be individually convolved with the PSF. As in R97, we do the convolution for each velocity slice efficiently by multiplications in Fourier space, using Fast Fourier Transforms (e.g., Press et al. 1992).

Kinematical data is generally obtained either through small, discrete apertures, along a number of slit-positions, or may derive from two-dimensional integral field spectroscopy (e.g., Bacon et al. 1995). Any setup of this kind can be simulated by our models, including possible spatial binning along a slit. For each observational ‘aperture’, we choose the  $(x', y', v_{\text{los}})$  cube with the most appropriate cell size, convolve it with the relevant PSF, and bin the results spatially over the aperture size. This yields a one-dimensional velocity histogram, for each orbit and for each observation. Examples of such ‘orbital VPs’ are shown in Figure 4.

Kinematical observations provide information on the line-of-sight VPs

$$\text{VP}(x', y', v_{\text{los}}) = \iiint \text{DF} dv_{x'} dv_{y'} dz', \quad (4)$$

at different positions  $(x', y')$  on the projected face of a galaxy. In practice, the normalization of  $\text{VP}(x', y', v_{\text{los}})$  is based on the photometric data. It is often useful to parametrize observed VPs by a few numbers. A common choice for such a VP parametrization is the Gauss-Hermite expansion. We follow the notation of vdMF, in which the VP is represented as

$$\text{VP}(v_{\text{los}}) = \frac{\alpha(w)}{\sigma} \sum_{l=0}^N h_l H_l(w), \quad (5)$$

with

$$w = (v_{\text{los}} - V)/\sigma, \quad \alpha(w) = \frac{1}{\sqrt{2\pi}} e^{-w^2/2}. \quad (6)$$

The  $h_l$  are the Gauss-Hermite moments (hereafter GH-moments) defined by

$$h_l = 2\sqrt{\pi} \int_{-\infty}^{\infty} \text{VP}(v_{\text{los}}) \alpha(w) H_l(w) dv_{\text{los}} \quad (l = 0, \dots, L). \quad (7)$$

Each  $H_l$  is a Hermite polynomial (see Appendix A of vdMF). The quantities  $V$  and  $\sigma$  characterize the ‘weighting function’,  $\alpha(w)H_l$ , in the integral (7). When describing observations,  $V$  and  $\sigma$  are usually taken to be the velocity and dispersion of the Gaussian that best fits the observed VP. With this choice,  $h_1 \equiv h_2 \equiv 0$ . GH-moments of higher order describe deviations from a Gaussian.

Only the moments of order  $L \leq 6$  are generally measured from galaxy spectra, due to the finite spectral (and thus velocity) resolution of the observations.

If we envision galaxies as consisting of orbital building blocks, then the overall VP measured for a given observation is just the superposition of the individual orbital VPs. Similarly, the observed GH-moments are just a linear superposition of the GH-moments of the individual orbital VPs, provided that the observed  $V$  and  $\sigma$  for the given observation are used in the weighting function  $\alpha(w)H_l(w)$ . Thus, as described in detail in R97, to fit the kinematical observations we may restrict ourselves to solving a linear superposition problem for the Gauss-Hermite moments. The constraints are then that  $h_1 = h_2 = 0$ , and the  $h_l$  with  $l \geq 3$  should equal their observed values. It must be stressed that this approach is general, and assumes neither that the observed VPs are well-described by the lowest-order terms of a GH-series, nor that the orbital VPs are well-described by the lowest-order terms of a GH-series. Nonetheless, if a full non-parametric estimate of the observed VPs is available there is no need to restrict the analysis to the lowest-order GH-moments. Our technique can just as easily fit the individual velocity bins of the observed VPs.

## 2.6. Fitting the Constraints

Constructing a model consists of finding a weighted superposition of the stellar orbits in the library that reproduces two sets of constraints:

- **Consistency constraints** for the stellar luminosity distribution. The model should reproduce the initially assumed luminous stellar density  $\rho_*(R, z)$  (Section 2.1), for each cell of the meridional  $(r, \theta)$  grid, for each cell of the projected plane  $(r', \theta')$  grid, and for each aperture for which there is kinematical data. In theory, it is sufficient to fit only the meridional plane masses, because projected densities are then fit automatically. In practice this might not exactly be the case, because of discretization. To circumvent this, the projected masses may be included as separate constraints. Note that for axisymmetric models the projected density does not uniquely specify the intrinsic density (e.g., Rybicki 1986; Gerhard & Binney 1996).
- **Kinematical constraints.** The model should reproduce the observed kinematics of the galaxy, including VP shapes. As discussed, we express this as a set of linear constraints on the GH-moments of the VPs (R97).

Finding the orbit superposition that best fits these constraints amounts to solving a linear problem, which can be written in matrix notation as  $\mathbf{B}\vec{\gamma} = \vec{c}$  (R97). The matrix  $\mathbf{B}$  contains the mass that each orbit contributes to each relevant intrinsic or projected grid cell, and the GH-moments that each orbit contributes to each kinematical observation. The vector  $\vec{c}$  contains the mass predicted by  $\rho_*(R, z)$  for each relevant intrinsic or projected grid cell, and the observed GH-moments for all kinematical observations; the vector  $\vec{\gamma}$ , which is to be solved for, contains the weight of each orbit, i.e., the total mass of stars on each orbit. These weights should be

non-negative. Using the terminology introduced in Section 2.5, the basic Schwarzschild equation becomes

$$\sum_{j=1}^{N_{\text{orbits}}} \gamma_j \text{VP}_{ij} = \text{VP}_i, \quad (8)$$

with  $\text{VP}_{ij}$  the individual VP of orbit  $j$  at constraint point  $i$ , and  $\text{VP}_i$  the observed VP for the same constraint point.

The superposition problem can be expressed as a non-negative least squares (NNLS) fit for the above matrix equation. We have used the NNLS routine of Lawson & Hanson (1974) to solve it. The NNLS routine finds a combination of non-negative orbital occupancies (which need not be unique) that minimizes the usual  $\mathcal{L}^2$  norm  $\|\mathbf{B}\vec{\gamma} - \vec{c}\|$ . This norm can be viewed as a  $\chi^2$  quantity that measures the quality of the fit to the constraints. The NNLS routine always finds a best solution. It need not be acceptable in light of the observations; this must be assessed through the  $\chi^2$  of the best fit, and by comparison of the model predictions to the constraints.

As is customary in least-squares fitting, the model predictions for each constraint and the actual constraint values (the elements of the vector  $\vec{c}$ ) are weighted by the errors in the constraints. Observational errors are available for the kinematical constraints. In principle one would like the consistency constraints to be fit with machine precision. It turns out that this is generally unfeasible, because of discretization. It was found that models with no kinematical constraints could at best simultaneously fit both the intrinsic and the projected masses with a fractional error of  $\sim 5 \times 10^{-3}$  (when using  $\sim 1000$  orbits). We therefore assigned fractional errors of this size to the masses in the consistency constraints. In principle one would like to include also the observational surface brightness errors in the analysis. Unfortunately, this requires the exploration of a large set of three-dimensional mass densities (that all fit the surface photometry to within the errors), which is prohibitively time-consuming.

## 2.7. Regularization

Our orbit superposition models are not generally smooth in integral space, as a result of the ‘ill-conditioned’ numerical nature of the NNLS matrix equation that is being solved. There are no physical theories that describe exactly how smooth the DF of a stellar system should be, but some degree of smoothness should be expected. Our technique can be extended in a straightforward manner to yield smooth solutions, by adding linear regularization constraints to the NNLS matrix equation (e.g., Press et al. 1992; Merritt 1993). This has the same effect as the addition of ‘maximum entropy’ constraints (Richstone & Tremaine 1988). For linear regularization, each regularization constraint must be of the form

$$\sum_k s_{k,l} \gamma_k = 0 \pm \Delta, \quad (9)$$

thus providing an extra row to the matrix equation. The  $\gamma_k$  are the orbital weights that make up the vector  $\vec{\gamma}$ , and  $l$  is the number of the regularization constraint. The parameter  $\Delta$  sets the amount of regularization. Models with  $\Delta \rightarrow \infty$  have no regularization, while models with  $\Delta \rightarrow 0$

give infinite weight to the regularization constraints. Alternatively, one may view this as adding a term  $\lambda \|\mathbf{S}\vec{\gamma}\|$  to the norm  $\|\mathbf{B}\vec{\gamma} - \vec{c}\|$  that is minimized by the NNLS routine, where  $\mathbf{S}$  is the matrix with elements  $\{s_{k,l}\}$ , and  $\lambda \equiv 1/\Delta$  is a regularization parameter (Zhao 1996b).

Many choices are possible for the matrix  $\mathbf{S}$ , with the only requirement that the norm  $\|\mathbf{S}\vec{\gamma}\|$  should provide a measure of the smoothness of the solution. Our choice is based on the fact that we consider the NNLS solution  $\gamma(R_c, \eta, R_{zvc})$  to be “smooth” if the second derivatives of the (unitless) function  $\gamma(R_c, \eta, R_{zvc})/\gamma_0(R_c)$  are small. Here the “reference weights”  $\gamma_0(R_c)$  are a rough approximation to the energy dependence of the model. These are determined beforehand, e.g., by studying the spherical isotropic limit of the given mass density. We view the three-dimensional numerical grid in integral space as a Cartesian lattice, and we approximate the second derivatives by second order divided differences (eq. 18.5.10 of Press et al. 1992). We assume that the distance between adjacent grid points on the lattice is unity, independent of the cartesian direction in which they are adjacent. This (arbitrarily) solves the problem that the axes of the grid in integral space have different units and yields three regularization constraints for each grid point  $(i, j, l)$  that is not on a boundary:  $-\gamma_{i-1,j,l} + 2\gamma_{i,j,l} - \gamma_{i+1,j,l} = 0$ ,  $-\gamma_{i,j-1,l} + 2\gamma_{i,j,l} - \gamma_{i,j+1,l} = 0$ , and  $-\gamma_{i,j,l-1} + 2\gamma_{i,j,l} - \gamma_{i,j,l+1} = 0$ .

### 3. Two-integral Components and Isotropic Components

#### 3.1. Definition

Individual regular orbits correspond to building blocks with a DF proportional to  $\delta(E - E_0) \delta(L_z - L_{z,0}) \delta(I_3 - I_{3,0})$ , for given  $(E_0, L_{z,0}, I_{3,0})$ . These are not the only building blocks that can be used to construct models. One may also use ‘two-integral components’, which correspond to the DF

$$f_{[E_0, L_{z,0}]}^\delta \equiv C_{[E_0, L_{z,0}]} \delta(E - E_0) \delta(L_z - L_{z,0}), \quad (10)$$

or ‘isotropic components’, which correspond to the DF (cf. Richstone 1982)

$$f_{[E_0]}^\delta \equiv C_{[E_0]} \delta(E - E_0). \quad (11)$$

We choose the normalization coefficients  $C_{[E_0, L_{z,0}]}$  and  $C_{[E_0]}$  such that the total mass of each component is equal to unity; explicit expressions are derived in Appendix A.1.

The two-integral components are smoother building blocks than the regular orbits, since they fill completely the ZVC and do not have the sharp edges of the regular orbits. It is useful to view them as a particular combination of all orbits that could be numerically integrated at the given  $(E_0, L_{z,0})$ , both regular orbits that fill only a subset of the area enclosed by the ZVC (therefore admitting 3 independent integrals of motion) *and* irregular orbits that occupy a larger area (admitting only 2 integrals; note that an irregular orbit does not necessarily fill the entire phase-space region defined by  $(E_0, L_{z,0})$ ; see Merritt & Valluri 1996 for a discussion of the triaxial case). Similarly, an isotropic component is a weighted combination of all two-integral components (i.e., all orbits) at the given energy  $E_0$ . The region in space occupied by such a component is bounded by the equipotential surface  $\Phi(R, z) = E_0$ .

The two-integral and isotropic components are useful, because their properties can be calculated semi-analytically. By using *only* two-integral components in the NNLS orbit superposition, one can construct  $f(E, L_z)$  models for arbitrary spheroidal potentials. This provides a new and convenient way of constructing such models, which adds to the several techniques already in existence for this purpose (Hunter & Qian 1993; Dehnen & Gerhard 1994; Kuijken 1995; Magorrian 1995; M96b). Using only isotropic components in the NNLS orbit superposition is generally less useful, because these components follow equipotential surfaces, which are rounder than isodensity surfaces. Thus, they cannot be used to build self-consistent isotropic axisymmetric models. R97 describe how to use them to build spherical isotropic models. Alternatively, the two-integral and isotropic components may be used in the superposition *in conjunction with* the regular orbits. This has two advantages. First, these components are smoother, and their inclusion therefore reduces numerical noise that arises from the discrete representation of phase space (see also Zhao 1996b). Second, addition of these components provides a way to include all irregular orbits in the models.

### 3.2. Velocity Profiles

The VP of a two-integral component is obtained by substitution of the DF of equation (10) into equation (4). The resulting integral may be written as

$$\text{VP}_{[E_0, L_{z,0}]}(x', y', v_{\text{los}}) = C_{[E_0, L_{z,0}]} \int dz' J_{[E_0, L_{z,0}]}, \quad (12)$$

where

$$J_{[E, L_z]} \equiv \left| \frac{\partial(v_{x'}, v_{y'})}{\partial(E, L_z)} \right|_{[E, L_z]}, \quad (13)$$

is the Jacobian for the change of variables from  $(v_{x'}, v_{y'})$  to  $(E, L_z)$ . In Appendix A.2 we give an explicit expression for this Jacobian. The integration in equation (12) extends over those  $z'$  for which there exist velocities  $(v_{x'}, v_{y'})$  such that  $E(x', y', z', v_{x'}, v_{y'}, v_{\text{los}}) = E_0$  and  $L_z(x', y', z', v_{x'}, v_{y'}, v_{\text{los}}) = L_{z,0}$ . Similarly, the VP for an isotropic component may be written as

$$\text{VP}_{[E_0]}(x', y', v_{\text{los}}) = C_{[E_0]} \int dz' \int dL_z J_{[E_0, L_z]}. \quad (14)$$

The projected density for a two-integral or isotropic component, at projected position  $(x', y')$ , is obtained as the integral of  $\text{VP}(x', y', v_{\text{los}})$  over  $v_{\text{los}}$ .

Equations (12) and (14) can be used to calculate the VPs of the two-integral and isotropic components through numerical quadratures, without the need for calculating orbital trajectories. The only difficulty lies in finding the domain of integration in  $z'$ . We illustrate this for the case of an edge-on system ( $i = 90^\circ$ ). In this case  $J_{[E_0, L_{z,0}]} = (z' v_{y'})^{-1}$ , with

$$v_{y'} = \sqrt{2(E_0 - \Phi) - \left( \frac{L_{z,0} + x' v_{\text{los}}}{z'} \right)^2 - v_{\text{los}}^2} \quad (15)$$

(cf. eqs. [A13,A14]). We will refer to the expression under the square-root as  $W$ . The integration in equation (12) extends over those  $z'$  for which  $W \geq 0$ . We find the roots of  $W$  numerically. We start by finding the roots of  $2(E_0 - \Phi) - v_{\text{los}}^2 = 0$ . This gives an interval that encompasses *all* real roots of  $W$ , because  $2(E_0 - \Phi) - v_{\text{los}}^2 \geq W$ . Then we subdivide this interval in many ( $\sim 100$ – $1000$ ) small segments, and check whether the sign of  $W$  differs at the ends of each segment. If it does, we find the root between these two points through bisection. The continuity of the resulting VP was used to check whether all required integration domains in  $z'$  were found. For the potentials studied here, we typically find two or four roots.

The VP calculation for edge-on *isotropic* components is less complicated. The Jacobian is quadratic in  $L_z$ , and can be written as  $J_{[E_0, L_z]} = [(L_z^+ - L_z)(L_z - L_z^-)]^{-1/2}$ . One can show that  $L_z^-$  and  $L_z^+$  are real if  $2(E_0 - \Phi) - v_{\text{los}}^2 \geq 0$ . In this case the integral over  $dL_z$  in equation (14) extends from  $L_z^-$  to  $L_z^+$ , and is always equal to  $\pi$ . Thus, if there is a  $z'_{\text{max}}$  for which  $2(E_0 - \Phi) - v_{\text{los}}^2 = 0$ , then

$$\text{VP}_{[E_0]}(x', y', v_{\text{los}}) = 2\pi C_{[E_0]} z'_{\text{max}}. \quad (16)$$

If there is no such  $z'_{\text{max}}$  (i.e., if  $v_{\text{los}}$  exceeds the escape velocity at the tangent point), then  $\text{VP}_{[E_0]}(x', y', v_{\text{los}}) = 0$ .

Figure 5 shows examples of the VP of a two-integral component along the major and minor axes of an edge-on system.

## 4. Tests

### 4.1. The Test Model

The most useful tests for our axisymmetric implementation are those for which the results can be compared to analytical results, or to semi-analytical or numerical results that were obtained with an independent algorithm. Models with  $f(E, L_z)$  DFs have been widely studied in the past five years (e.g., Evans 1993, 1994; Hunter & Qian 1993; Dehnen & Gerhard 1994; Evans & de Zeeuw 1994; Kuijken 1995; Q95; Magorrian 1995; M96b). Their properties can be derived semi-analytically, and a variety of algorithms and numerical implementations have been presented to derive the DF  $f(E, L_z)$  that generates a given luminous mass density  $\rho_*(R, z)$  in a given potential  $\Phi(R, z)$ . These models therefore provide an ideal test case. Here we present two tests where we use our method to reproduce the properties of an edge-on  $f(E, L_z)$  model.

We consider a model with a luminous mass density of the form (1), with parameters:  $\alpha = -1.435$ ,  $\beta = -0.423$ ,  $\gamma = \epsilon = 2.0$ ,  $\delta = -1.298$ ,  $b = 0.55''$ ,  $c = 102.0''$ ,  $q = 0.73$ ,  $\rho_0 = j_0 \Upsilon M_\odot / L_{\odot, V}$ ,  $j_0 = 0.463 \times 10^5 L_{\odot, V} \text{pc}^{-3}$  (for an assumed distance of 0.7 Mpc). We calculate the potential of the test model,  $\Phi \equiv \Phi_* + \Phi_{\text{dark}}$ , under the assumption that  $\Upsilon = 2.5$ , and with the option of a nuclear BH ( $\Phi_{\text{dark}} = -GM_{\text{BH}}/r$ ) of mass  $M_{\text{BH}} = 3 \times 10^6 M_\odot$ . All these parameters are based on the application of our technique to the case of the galaxy M32, which was presented in vdM98. This analogy with M32 was chosen mainly to demonstrate the accuracy of our method for a realistic galaxy model.

The luminous mass density  $\rho_*(R, z)$  and potential  $\Phi(R, z)$  determine uniquely only the even part  $f_{\text{even}}(E, L_z)$  of the DF,  $f(E, L_z) \equiv f_{\text{even}}(E, L_z) + f_{\text{odd}}(E, L_z)$ . For our test model we specify (arbitrarily) the extreme case that  $f_{\text{odd}}(E, L_z) = f_{\text{even}}(E, L_z)$  for  $L_z > 0$ , and that  $f_{\text{odd}}(E, L_z) = -f_{\text{even}}(E, L_z)$  for  $L_z < 0$  (and by definition,  $f_{\text{odd}}(E, 0) = 0$ ). Thus, the  $f(E, L_z)$  test model is ‘maximally rotating’: all the stars are rotating in the same sense and have  $L_z > 0$ .

First, the unique  $f(E, L_z)$  DF of the test model was calculated using the approach described in vdM98. We will refer to the resulting DF as  $\text{DF}_{\text{HQ}}$  (for Hunter & Qian, 1993). The kinematical predictions (VPs, GH-moments, etc.) for the test model DF were subsequently calculated using the expressions and software of Q95. The Jeans equations were used as in Cretton & van den Bosch (1999) to compute the intrinsic second-order velocity moments  $\langle v_\phi^2 \rangle$  and  $\langle v_r^2 \rangle = \langle v_\theta^2 \rangle$  in the meridional plane. Our tests in Sections 4.2 and 4.3 are aimed at assessing how well our algorithm can reproduce the test model properties thus calculated with independent methods. This allows us to test all key aspects of the orbit model construction, including the sampling of integral space, orbit calculation, discreteness effects of the spatial grids, projection into the data cubes, seeing convolution, and the NNLS algorithm. Hence, it is no great drawback that our tests are restricted to two-integral models.

#### 4.2. Reproducing the Test Model with Two-integral Components

We first describe tests of the extended Schwarzschild technique with only two-integral components. We used an  $(E, L_z)$  grid as described in Section 2.2, with  $N_E = 70$ ,  $R_{c,\text{min}} = 10^{-4.2}$  arcsec,  $R_{c,\text{max}} = 10^{4.2}$  arcsec,  $N_\eta = 19$ , and  $\epsilon_1 = 0.01$ . Only components with  $L_z > 0$  were included in the superposition; the resulting models are therefore by definition maximally rotating with a DF of the form  $f(E, L_z)$ . The DF is determined uniquely by the mass density. Kinematical constraints are therefore not required in the NNLS fit, but only constraints on the consistency of the stellar luminosity distribution (see Section 2.6). For these, the polar  $(r, \theta)$  and  $(r', \theta')$  grids in the meridional plane and on the projected plane of the sky (see Section 2.4) were chosen to have 16 bins in the radial coordinate between  $R_{c,\text{min}}$  and  $R_{c,\text{max}}$ , and  $N_\theta = N_{\theta'} = 7$  bins in the angular coordinate (a rather modest resolution, but similar tests with finer grids yielded similar accuracies). We semi-analytically (eq. [4-140b] of BT) calculated the isotropic DF  $f(E)$  for the spherical version of the test model, and used the corresponding masses on our energy grid as reference weights for the regularization (see Section 2.7).

The NNLS algorithm yields the mass on each  $(E, L_z)$  grid cell, i.e., the integral of  $dM / dE dL_z$  over the grid cell. It does *not* directly yield the DF  $f(E, L_z)$ , which by definition is the density in the six dimensional phase-space. However, for a two-integral model there is a simple relation between  $dM / dE dL_z$  and the DF  $f(E, L_z)$ , as derived in Appendix B.1. With equation (B3) the NNLS fit provides an estimate of the DF, which we will denote  $\text{DF}_{\text{NNLS}}$ . We compare it with  $\text{DF}_{\text{HQ}}$  on the same grid, but to avoid possible border effects, we restrict the comparison to the  $N_E = 50$  energy grid points with  $R_c$  between  $10^{-3}$  and  $10^3$  arcsec (see Figures 6 and 7 for the test models with and without a central BH, respectively).

The DFs agree well over 10 and 20 orders of magnitude, respectively. The inserts show the percentage errors in the DF calculation. Note that the largest errors occur at grid points that carry little mass, e.g., at large radii. The orbit library in these figures is numbered as follows. For each value of  $R_c(E)_j$  of the energy,  $L_z$  runs monotonically from  $L_{z,\min}$  to  $L_{z,\max}$ , covering  $N_\eta$  ( $= 19$  here) components. The next orbit corresponds to  $L_{z,\min}$  of  $R_c(E)_{j+1}$ , etc. This choice of numbering causes the jagged appearance of the DF. Q95 plotted  $f(E, L_z = 0)$  and  $f(E, L_z = L_{z,\max})$  as a function of  $E$  (see their Figure 8), and such curves would appear as envelopes in Figures 6 and 7.

To assess the influence of smoothing on the accuracy with which our technique recovers the DF, we have studied the dependence of the RMS logarithmic residual

$$\text{RMS}_{\log \text{DF}} \equiv \left[ \frac{1}{N_E N_\eta} \sum_{i=1}^{N_E} \sum_{j=1}^{N_\eta} (\log \text{DF}_{\text{NNLS}} - \log \text{DF}_{\text{HQ}})^2 \right]^{1/2}, \quad (17)$$

on the regularization parameter  $\Delta$  (see Section 2.7). When  $\Delta$  tends to zero, the regularization constraints receive infinite weight. This yields a very smooth DF, but one that doesn't fit the consistency (mass) constraints very well, and therefore doesn't approximate  $\text{DF}_{\text{HQ}}$  very well. At the other extreme, when  $\Delta$  is very large there is hardly any smoothing, and the mathematically ill-conditioned nature of the problem yields a very jagged solution that also doesn't match  $\text{DF}_{\text{HQ}}$ . Figure 8 shows  $\text{RMS}_{\log \text{DF}}(\Delta)$  for the following three cases: (a) the case in which only the masses on the meridional plane ( $r, \theta$ ) grid are included as constraints in the NNLS fit; (b) the case in which only the masses on the projected plane ( $r', \theta'$ ) grid are included as constraints; and (c) the case in which both are included as constraints. In principle, deprojection of the projected mass density is unique for an edge-on system, so these approaches should recover equivalent results. However, this is not true in practice because of discretization effects. In all three cases,  $\text{RMS}_{\log \text{DF}}$  has a minimum near  $\log \Delta \approx 2.0$ , which is thus the optimum smoothing. The value of  $\text{RMS}_{\log \text{DF}}$  at the minimum is only mildly different for the different cases, but (a) yields the slightly better results. We have therefore adopted case (a) for all our further test calculations. The minimum  $\text{RMS}_{\log \text{DF}}$  is  $\sim 0.02$ ; this corresponds to a 5% RMS difference between  $\text{DF}_{\text{NNLS}}$  and  $\text{DF}_{\text{HQ}}$ . The mass-weighted RMS difference,

$$\text{RMS}_{\text{DF}} = \left[ \iint \text{DF}_{\text{HQ}} \left[ \frac{\text{DF}_{\text{NNLS}} - \text{DF}_{\text{HQ}}}{\text{DF}_{\text{HQ}}} \right]^2 d^3 \vec{x} d^3 \vec{v} / \iint \text{DF}_{\text{HQ}} d^3 \vec{x} d^3 \vec{v} \right]^{1/2}, \quad (18)$$

for the model with the optimum smoothing is also  $\sim 5\%$ . This level of accuracy in the determination of the DF is similar to that obtained with other techniques (see Gerhard et al. 1998; Matthias & Gerhard 1999).

Figure 9 compares the predictions for the meridional plane velocity moments to the results of the Jeans equations, for the model without a BH and with the optimum smoothing. The top and bottom row of the figure show  $\langle v_\phi^2 \rangle^{1/2}$  and  $\langle v_r^2 \rangle^{1/2} = \langle v_\theta^2 \rangle^{1/2}$ , respectively. We plot separately each angular sector of the polar grid in the meridional plane. In each row, the first panel is closest to the symmetry axis and the last one is closest to the equatorial plane. Full lines show predictions of the extended Schwarzschild technique, and dashed lines the results obtained from



the Jeans equations. The model predictions were interpolated between the  $(E, L_z)$  grid points to get smoother results. Overall the agreement is very good, and better than 1%. This is better than the  $\sim 5\%$  agreement in the DF, because the velocity moments are integrals over the DF (such that errors tend to cancel). The errors in the velocity moments are largest near the symmetry axis, since in the extended Schwarzschild technique only a few components with very low  $L_z$  can reach this region of the meridional plane. However, the errors are always  $\lesssim 2 \text{ km s}^{-1}$ .

### 4.3. Reproducing the Test Model with Regular orbits

The next step in our testing procedure is to try to reproduce the properties of the test model with regular orbits, rather than two-integral components. The first obvious question is whether we can give the orbit superposition algorithm constraints that force it to generate a model with a DF of the form  $f(E, L_z)$ , which can then be compared to the distribution function  $\text{DF}_{\text{HQ}}$  calculated as in Section 4.1. Unfortunately, there is no set of simple linear kinematic constraints that force the NNLS algorithm to produce an  $f(E, L_z)$  model. One can certainly impose the necessary conditions that  $\langle v_r^2 \rangle = \langle v_\theta^2 \rangle$  and  $\langle v_r v_\theta \rangle = 0$ , but these conditions are not sufficient; an  $f(E, L_z)$  model is fully determined only by constraints on *all* its higher order velocity moments (e.g., Magorrian & Binney 1994).

We therefore restrict ourselves here to a simpler test. We calculate an orbit library in the gravitational potential of the test model, but do not do a subsequent NNLS fit. Instead, we fix the orbital weights  $\gamma_j$  to those appropriate for an  $f(E, L_z)$  model, and merely calculate the projected kinematical quantities for some observational test setup, given these orbital weights. The results are compared to the same quantities but now calculated from  $\text{DF}_{\text{HQ}}$  as described in Section 4.1. This tests all of the important parts of our method that were not already tested by the calculations in Section 4.2, namely the orbit calculation, the projection into data cubes and VPs, and the seeing convolution.

The main difficulty with this test is that it requires knowledge of the orbital weights for an  $f(E, L_z)$  model, i.e., of the differential mass density  $dM / dE dL_z dR_{zvc}$ , on the grid of quantities  $(E, L_z, R_{zvc})$  that we use to sample orbit space (cf. Section 2.2). This is not as straightforward as the calculation of  $dM / dE dL_z$  described in Appendix B.1. In fact, the orbital weights can only be easily calculated if an explicit expression exists for the third integral, which is not the case for our test model. However, if the model has a central BH then at small radii, or high energies, the potential is Keplerian and spherical (as it is at large radii, or low energies, because of the finite mass of the model). In this potential, all the integrals of motion are known, and these limits are therefore analytically tractable.

At high energies (small radii) the test model reduces to a scale-free axisymmetric mass density cusp with an  $f(E, L_z)$  DF in a spherical Kepler potential. This limit was studied analytically by de Bruijne, van der Marel & de Zeeuw (1996). In this limit, the normalized distribution of mass over  $(\eta, R_{zvc}/R_c)$  at fixed energy, which we will denote as  $h(\eta, R_{zvc}/R_c)$ , is a known function that is independent of energy. An explicit expression for  $h(\eta, R_{zvc}/R_c)$  is derived in Appendix B.2. We

use this result to approximate the differential mass density of our test model, restricting ourselves to the case with a  $3 \times 10^6 M_\odot$  BH. First, we calculate the differential mass density of the model over energy alone:  $G(E) \equiv dM / dE = \int [dM / dE dL_z] dL_z$ ; where  $dM / dE dL_z$  is obtained from equation (B3). Then, we assume that the distribution of mass over  $(L_z, R_{zvc})$  at fixed energy is always the same as in the high-energy limit, so that

$$\frac{dM}{dE d\eta d(R_{zvc}/R_c)} = G(E) h(\eta, R_{zvc}/R_c). \quad (19)$$

This relation is only correct at asymptotically high energies. We found it was sufficiently good at energies with  $R_c(E) \lesssim 0.5''$ , which is where the mass density of the model is a pure power law and where the potential is Keplerian.

For our test we picked an observational test-setup with the same set of 8 square apertures, roughly aligned on the major axis, as used by van der Marel et al. (1997b) in their HST observations of M32 (see their Figure 3). These apertures all lie at projected radii  $R \lesssim 0.5''$ , so most of the light seen in these apertures originates from stars with energies for which our approximation of the differential mass distribution is adequate. We chose the same PSF as in van der Marel et al. (1997b), which is a sum of three Gaussians that approximates the HST PSF. Subsequently, we picked a grid in  $(E, L_z, R_{zvc})$  space with  $N_E = 20$ ,  $N_\eta = 7$ , and  $N_{I_3} = 7$ , and we calculated an orbit library for this grid. Then finally we calculated orbital weights from equation (19), by integrating at each point of our  $(E, L_z, R_{zvc})$  grid the approximation  $dM / [dE d\eta d(R_{zvc}/R_c)]$  over the corresponding grid cell. Predictions for the projected kinematics then follow by superposing the VPs for individual orbits in the library as in equation (8).

Figure 10 shows the results thus obtained for the kinematical quantities  $V, \sigma, h_3, \dots, h_6$ . As mentioned in Section 1, independent software implementations of the extended Schwarzschild method were programmed by both N.C. and R.v.d.M. Dotted curves in the figure show the results from N.C.’s software, while dashed curves show the results from R.v.d.M.’s software. For comparison, solid curves show the results obtained by direct integration over the known  $DF_{\text{HQ}}$ , using the (completely independent) software of Q95 as described in Section 4.1. The RMS difference between the different predictions is  $\sim 2 \text{ km s}^{-1}$  in  $V$  and  $\sigma$ , and  $\sim 0.01$  in the Gauss-Hermite moments. Kinematical data typically have larger observational errors than this, so the numerical accuracy of our method is entirely adequate for modeling real galaxies.

Finally, let us say a few words about the orbits in the library for this test model. Figure 11 shows the orbits in the library at the energy corresponding to  $R_c = 0.25''$ . Figure 12 shows the orbits at the same  $R_c$ , in the same model, but now without a BH. The orbits are all regular and have a stable periodic parent. The parents were determined using surfaces-of-section (see also: Richstone 1982; Lees & Schwarzschild 1992; Evans 1994; Evans, Häfner & de Zeeuw 1997) and are indicated in the figures. Most orbits in Figures 11 and 12 are tubes, and are parented by the thin tube. Orbits that are not tubes are indicated. A minority of the low  $|\eta|$  orbits in Figure 12 is parented by higher-order resonances, such as the 3:2 and 4:3 (being the ratio of the  $R$ - and  $z$ -frequencies of the parent). By contrast, most of the low  $|\eta|$  orbits in Figure 11 is parented by the 1:1 resonance. Thus the orbital structure of the models with and without BH is very clearly different. An analysis of the orbital structure of these models as a function of the BH mass is

beyond the scope of the present paper, but does seem worth further study.

## 5. Concluding Remarks

In this paper we have described an extension of Schwarzschild’s method for building anisotropic axisymmetric dynamical models of galaxies. We compute a set of orbits in a given mass model and find the non-negative superposition of these orbits that best reproduces a set of (photometric and kinematic) constraints. Our method includes the full VP shape as kinematic constraint. We parametrize the VP using a GH expansion so that it is specified by a few numbers. The modeling method is valid for any kind of parametric (or non-parametric) VP representation and properly takes into account the observational setup (seeing convolution, pixel binning, error on each constraint). We obtain smooth models by imposing a regularization scheme in integral-space.

R97 have described in detail several aspects of this method and applied it to the spherical case. However, it is not restricted to this simple geometry, and we have described here the axisymmetric extension. The mass model used to compute the orbit library may be complex: it can have a central density cusp, a stellar disk, a central black hole or an extended dark halo. Applications of our code to the flattened systems M32 and NGC 4342 were presented in vdM98 and Cretton & van den Bosch (1999).

We have also devised a new semi-analytic method for constructing simpler dynamical models, for which the DF has the special form  $DF = f(E, L_z)$  or  $DF = f(E)$ . These DFs are obtained by using NNLS with analytic building blocks for which the VPs are obtained by one-dimensional quadratures. This technique is general and does not require the density to be expressed analytically as a function of the potential, but can be used with any complex mass model. Previous techniques assuming  $DF = f(E, L_z)$  that are also free of this condition include those of Hunter & Qian (1993), Dehnen & Gerhard (1994), Kuijken (1995), Magorrian (1995) and M96b.

We have tested our new method by having it reproduce the properties of  $f(E, L_z)$  models for which the DF and projected properties can be calculated with independent algorithms. This allowed us to test all aspects of the superposition method, including the sampling of integral space, orbit calculation, discreteness effects of the spatial grids, projection into the data cubes, seeing convolution, and the NNLS algorithm. Tests with only two-integral components reproduced the DF with a mass-weighted RMS accuracy of  $\lesssim 5\%$ , and the meridional plane velocity moments to better than  $2 \text{ km s}^{-1}$ . Tests with a regular orbit library indicated accuracies in the projected quantities of  $\sim 2 \text{ km s}^{-1}$  in  $V$  and  $\sigma$ , and 0.01 in the GH-moments. All the tests that we have done indicate that the accuracy of our method is adequate for the interpretation of kinematical data obtained with realistic setups.

Our technique can be extended to triaxiality. Several parts of the method will be unaltered for this geometry: the use of projected quantities, e.g.,  $VP(x', y', v_{\text{los}})$ , the fitting procedure, the seeing convolution, etc. However, the orbital structure is much richer than in the axisymmetric case. New orbit families appear (e.g., box orbits) as well as numerous chaotic regions associated with resonances. During the numerical integration of a trajectory in such a mass model, all six

phase-space coordinates need to be computed, since there is no azimuthal symmetry. Consequently, the computing overhead is significantly higher for triaxial geometries. Work along these lines is in progress.

NC expresses his thanks to Richard Arnold for his help. It is a pleasure to thank Frank van den Bosch, Eric Emsellem, Hong-Sheng Zhao, Yannick Copin, Walter Jaffe and Luis Aguilar for fruitful discussions on the modeling technique. NC acknowledges the hospitality of MPA (Garching) and Steward Observatory, and thanks D. Pfenniger for discussions at initial stages of this project and visits to Geneva Observatory. He was financially supported by a grant from the Swiss government (Etat du Valais) and by an exchange grant from NUFFIC. He and PTdZ acknowledge travel support from the Leids Kerkhoven Bosscha Fonds. RPvdM was supported by NASA through grant number # GO-05847.01-94A, Hubble Fellowship # HF-1065.01-94A and an STScI Institute Fellowship, all awarded by the Space Telescope Science Institute which is operated by the Association of Universities for Research in Astronomy, Incorporated, under NASA contract NAS5-26555. PTdZ acknowledges the hospitality of the Institute for Advanced Study where this work was initiated.

## A. Construction of $f(E, L_z)$ - and $f(E)$ -components

### A.1. Normalization

To determine the normalization coefficients  $C_{[E_0, L_{z,0}]}$  and  $C_{[E_0]}$  in the definitions of the two-integral and isotropic components (eqs. [10, 11]), we seek expressions for the total mass of a single component. The phase-space volume in cylindrical coordinates is  $d^3\vec{x} d^3\vec{v} = R^2 dR d\phi dz d\dot{R} d\dot{\phi} d\dot{z}$ . We use

$$\dot{R}^2 = 2[E - \Phi(R, z)] - \frac{L_z^2}{R^2} - \dot{z}^2, \quad \dot{\phi} = L_z/R^2, \quad (\text{A1})$$

to switch, at fixed  $(R, z)$ , from the variables  $(\dot{R}, \dot{z})$  to  $(E, L_z)$ . We then find for the total mass of a two-integral component:

$$m_{[E_0, L_{z,0}]} \equiv \int d^3\vec{x} d^3\vec{v} f_{[E_0, L_{z,0}]}^\delta = \int R^2 dR \int d\phi \int dz \int \frac{dE}{\dot{R}} \int \frac{dL_z}{R^2} \int d\dot{z} f_{[E_0, L_{z,0}]}^\delta. \quad (\text{A2})$$

Upon substitution of  $f_{[E_0, L_{z,0}]}^\delta$  from equation (10), the integration over  $\phi$ ,  $E$  and  $L_z$  becomes trivial, and we obtain

$$m_{[E_0, L_{z,0}]} = 4\pi C_{[E_0, L_{z,0}]} \iint dR dz \int \left\{ 2[E_0 - \Phi(R, z)] - \frac{L_{z,0}^2}{R^2} - \dot{z}^2 \right\}^{-1/2} d\dot{z}. \quad (\text{A3})$$

The integral over  $d\dot{z}$  extends over the region  $|\dot{z}| \leq \dot{z}_{\max}$ , where  $\dot{z}_{\max}$  is defined as the root of the expression in the square root. Therefore,

$$m_{[E_0, L_{z,0}]} = 8\pi C_{[E_0, L_{z,0}]} \iint dR dz \int_0^{\dot{z}_{\max}} \frac{d\dot{z}}{\sqrt{\dot{z}_{\max}^2 - \dot{z}^2}} = 4\pi^2 C_{[E_0, L_{z,0}]} \iint dR dz, \quad (\text{A4})$$

where the remaining double integral is over the region for which  $E_0 - \Phi(R, z) - (L_{z,0}^2/2R^2) \geq 0$ . This is exactly the region  $\Phi_{\text{eff},0}(R, z) \leq E_0$  bounded by the ZVC at the given  $(E_0, L_{z,0})$ , where  $\Phi_{\text{eff},0}$  is the effective gravitational potential at the given  $L_{z,0}$ . To obtain  $m_{[E_0, L_{z,0}]} = 1$ , we choose

$$C_{[E_0, L_{z,0}]} = \left[ 4\pi^2 \iint_{\Phi_{\text{eff},0}(R,z) \leq E_0} dR dz \right]^{-1} = \left[ 2\pi^2 \oint_{\text{ZVC}[E_0, L_{z,0}]} (R dz - z dR) \right]^{-1}, \quad (\text{A5})$$

where the second equality was obtained with a variant of Stokes' theorem.

Following similar arguments, we obtain for the mass of an isotropic component:

$$\begin{aligned} m_{[E_0]} &\equiv \int d^3\vec{x} d^3\vec{v} f_{[E_0]}^\delta \\ &= 8\pi C_{[E_0]} \iiint dR dz \int dL_z \int_0^{\dot{z}_{\max}} \frac{d\dot{z}}{\sqrt{\dot{z}_{\max}^2 - \dot{z}^2}} = 4\pi^2 C_{[E_0]} \iiint_{\Phi_{\text{eff}}(R,z) \leq E_0} dR dz dL_z, \end{aligned} \quad (\text{A6})$$

where the effective gravitational potential  $\Phi_{\text{eff}}(R, z)$  is a function of  $L_z$ , at fixed  $(R, z)$ . Evaluation of the integral over  $dL_z$  yields

$$m_{[E_0]} = 8\sqrt{2} \pi^2 C_{[E_0]} \int_{\Phi(R,z) \leq E_0} R \sqrt{E_0 - \Phi(R, z)} dR dz. \quad (\text{A7})$$

To obtain  $m_{[E_0]} = 1$ , we choose

$$C_{[E_0]} = \left[ 8\sqrt{2} \pi^2 \int_{\Phi(R,z) \leq E_0} R \sqrt{E_0 - \Phi(R,z)} \, dR \, dz \right]^{-1}. \quad (\text{A8})$$

For the special case of a spherical potential,  $\Phi = \Phi(r)$ , we have

$$m_{[E_0]} = 16\sqrt{2} \pi^2 C_{[E_0]} \int_{\Phi(r) \leq E_0} r^2 \sqrt{E_0 - \Phi(r)} \, dr, \quad (\text{A9})$$

which can be recognized as the ‘density-of-states’ function for an isotropic spherical system (BT). Calculations for spherical components with DFs proportional to  $\delta(E - E_0) \delta(L - L_0)$  were presented in Appendix A of R97.

## A.2. Velocity profiles

We derive here the Jacobian  $J$  for the transformation from  $(v_{x'}, v_{y'})$  to  $(E, L_z)$ , which enters into the expressions for the VPs of two-integral and isotropic components (eqs. [12,14]). The energy is

$$E = \frac{1}{2}(v_{x'}^2 + v_{y'}^2 + v_{\text{los}}^2) + \Phi(x', y', z'). \quad (\text{A10})$$

For inclination angle  $i$ ,

$$x = -y' \cos i + z' \sin i, \quad z = y' \sin i + z' \cos i, \quad (\text{A11})$$

and the angular momentum is therefore

$$L_z = xv_y - yv_x = v_{x'}(-y' \cos i + z' \sin i) + v_{y'}(x' \cos i) - v_{\text{los}}(x' \sin i). \quad (\text{A12})$$

This yields for the Jacobian

$$J = \left| x'v_{x'} \cos i + y'v_{y'} \cos i - z'v_{y'} \sin i \right|^{-1}, \quad (\text{A13})$$

in which  $v_{x'}$  and  $v_{y'}$  are functions of  $E$  and  $L_z$  determined by:

$$v_{x'} = \frac{L_z - v_{y'}x' \cos i + v_{\text{los}}x' \sin i}{-y' \cos i + z' \sin i}, \quad v_{y'}^2 = 2(E - \Phi) - v_{x'}^2 - v_{\text{los}}^2. \quad (\text{A14})$$

Substitution of  $v_{x'}$  in the expression for  $v_{y'}^2$  yields a quadratic equation for  $v_{y'}$ :

$$av_{y'}^2 + bv_{y'} + c = 0, \quad (\text{A15})$$

where

$$\begin{aligned} a &= (-y' \cos i + z' \sin i)^2 + (x' \cos i)^2, \\ b &= -2(L_z + v_{\text{los}}x' \sin i) x' \cos i, \\ c &= v_{\text{los}}^2(-y' \cos i + z' \sin i)^2 + (L_z + v_{\text{los}}x' \sin i)^2 - 2(E - \Phi)(-y' \cos i + z' \sin i)^2. \end{aligned} \quad (\text{A16})$$

Therefore,

$$v_{y'} = \frac{2(L_z + v_{\text{los}}x' \sin i) x' \cos i \pm \sqrt{\Delta}}{2[(-y' \cos i + z' \sin i)^2 + (x' \cos i)^2]}, \quad (\text{A17})$$

with  $\Delta \equiv b^2 - 4ac$ . Equations (A13), (A14) and (A17) define the Jacobian  $J$ .

## B. Relation Between Orbital Weights and the DF

### B.1. $dM/dE dL_z$ for an $f(E, L_z)$ model

For a two-integral model there is a simple relation between the differential mass density  $dM/dE dL_z$  and the DF  $f(E, L_z)$ . To derive this relation (see also Vandervoort 1984) we write the trivial identity

$$f(E, L_z) = \iint f(E_0, L_{z,0}) (f_{[E_0, L_{z,0}]}^\delta / C_{[E_0, L_{z,0}]}) dE_0 dL_{z,0}, \quad (\text{B1})$$

where  $f_{[E_0, L_{z,0}]}^\delta$  and  $C_{[E_0, L_{z,0}]}$  are as defined in equation (10). The total mass of the system is

$$M \equiv \int d^3\vec{x} d^3\vec{v} f(E, L_z) = \iint f(E_0, L_{z,0}) (m_{[E_0, L_{z,0}]} / C_{[E_0, L_{z,0}]}) dE_0 dL_{z,0}, \quad (\text{B2})$$

where the second identity follows upon substitution of equation (B1), exchange of the integration order, and use of the definition of  $m_{[E_0, L_{z,0}]}$  from equation (A2). Substitution of equations (A4) and (A5), relabeling of the integration variables from  $(E_0, L_{z,0})$  to  $(E, L_z)$ , and differentiation then yields

$$dM/dE dL_z = f(E, L_z) \times \left[ 2\pi^2 \oint_{\text{ZVC}[E, L_z]} (R dz - z dR) \right]. \quad (\text{B3})$$

The mass weight  $\gamma_j$  for a cell in integral space is

$$\gamma_j = \iint_{\text{cell}_j} \frac{dM}{dE dL_z} dE dL_z. \quad (\text{B4})$$

### B.2. Scale-free Density in a Kepler Potential

We summarize here the asymptotic case of a scale-free axisymmetric density in a spherical Kepler potential, which was discussed in detail by de Bruijne, van der Marel & de Zeeuw (1996). We adopt the same units as in that paper. In those units,  $\rho_\star = s^{-\xi}$  and  $\Psi = 1/r$ , where  $s$  is defined as in eq. (1) by  $s^2 = R^2 + (z/q)^2$ , with  $q$  the axial ratio. The associated eccentricity is  $e = \sqrt{1 - q^2}$ . It is convenient to work with the integrals of motion

$$\mathcal{E} = -E, \quad \eta^2 \equiv L_z^2 / L_{\text{max}}^2(\mathcal{E}), \quad \zeta^2 \equiv L^2 / L_{\text{max}}^2(\mathcal{E}), \quad (\text{B5})$$

where  $\mathcal{E}$  is the binding energy,  $\eta^2 \in [0, 1]$  and  $\zeta^2 \in [\eta^2, 1]$ . The unique (even) two-integral DF is

$$\text{DF}(\mathcal{E}, \eta^2) = C_0 g(\mathcal{E}) j(e^2 \eta^2), \quad (\text{B6})$$

where

$$C_0 = \frac{q^\xi}{2\pi \mathcal{B}(\xi - \frac{1}{2}, \frac{3}{2})}, \quad g(\mathcal{E}) = \mathcal{E}^{\xi - \frac{3}{2}}, \quad j(e^2 \eta^2) = {}_3F_2\left(\frac{\xi}{2}, \frac{\xi+1}{2}, \frac{\xi+2}{2}; \frac{1}{2}, \frac{2\xi-1}{2}; e^2 \eta^2\right). \quad (\text{B7})$$

The special functions  $\mathcal{B}$  and  ${}_3F_2$  are the beta-function and a generalized hypergeometric function, respectively. Upon substitution of  $\xi = -\alpha$  this yields the  $R_c \rightarrow 0$  limit of our test model (Section 4.1); upon substitution of  $\xi = -\alpha - (\beta\gamma) - (\delta\epsilon)$ , it yields the  $R_c \rightarrow \infty$  limit.

We wish to calculate the mass weight  $\gamma_j$  contained in a cell number  $j$  of integral space (see eq. [8]). According to equations (35) and (37) of de Bruijne et al., this is given by:

$$\gamma_j = \iiint_{\text{cell}_j} d\mathcal{E} d\eta^2 d\zeta^2 w(\mathcal{E}, \eta^2, \zeta^2) \text{DF}(\mathcal{E}, \eta^2), \quad w(\mathcal{E}, \eta^2, \zeta^2) = \frac{\pi^3}{4} \mathcal{E}^{-5/2} (\eta^2)^{-1/2} (\zeta^2)^{-1/2}. \quad (\text{B8})$$

In the Kepler potential the binding energy is related to the circular radius according to  $\mathcal{E} = 1/(2R_c)$ . The ZVC at a given  $(R_c, \eta^2)$  is therefore defined by

$$1 = \frac{2R_c}{r} - \left(\frac{R_c\eta}{R}\right)^2. \quad (\text{B9})$$

A particle on the ZVC has  $v_r = v_\theta = 0$ ,  $L^2 = r^2 v_\phi^2$  and  $L_z^2 = R^2 v_\phi^2$ . Therefore, we have  $\zeta^2 = (r\eta/R)^2$ . Combined with the expression for the ZVC this yields

$$\zeta^2 = \left[ \frac{2\eta (R_{\text{zvc}}/R_c)}{\eta^2 + (R_{\text{zvc}}/R_c)^2} \right]^2, \quad (\text{B10})$$

which is a one-to-one relation if  $(R_{\text{zvc}}/R_c)$  is chosen between  $\eta$  and  $1 + \sqrt{1 - \eta^2}$ . Substitution of the DF from equation (B6) into equation (B8), and transformation to the variables  $\log R_c$ ,  $\eta \in [0, 1]$  and  $(R_{\text{zvc}}/R_c) \in [\eta, 1 + \sqrt{1 - \eta^2}]$  yields

$$\frac{dM}{d(\log R_c) d\eta d(R_{\text{zvc}}/R_c)} = 2 C_0 \pi^3 \left(\frac{R_c}{2}\right)^{3-\xi} \eta j(e^2 \eta^2) \left\{ \frac{\eta^2 - (R_{\text{zvc}}/R_c)^2}{[\eta^2 + (R_{\text{zvc}}/R_c)^2]^2} \right\}. \quad (\text{B11})$$

Hence, the normalized distribution of mass over  $(\eta, R_{\text{zvc}}/R_c)$  at fixed energy, which we will denote as  $h(\eta, R_{\text{zvc}}/R_c)$ , is independent of energy. In particular:

$$h(\eta, R_{\text{zvc}}/R_c) = 2\eta j(e^2 \eta^2) \left\{ \frac{\eta^2 - (R_{\text{zvc}}/R_c)^2}{[\eta^2 + (R_{\text{zvc}}/R_c)^2]^2} \right\} / \int_0^1 d\eta^2 j(e^2 \eta^2) \int_\eta^{1+\sqrt{1-\eta^2}} d(R_{\text{zvc}}/R_c) \left\{ \frac{\eta^2 - (R_{\text{zvc}}/R_c)^2}{[\eta^2 + (R_{\text{zvc}}/R_c)^2]^2} \right\}. \quad (\text{B12})$$



## REFERENCES

- Bacon, R. et al. 1995, *A&AS*, 113, 247
- Binney, J. J., & Merrifield, M. R. 1998, *Galactic Astronomy* (Princeton: Princeton University Press)
- Binney, J. J., & Tremaine, S. D. 1987, *Galactic Dynamics* (Princeton: Princeton University Press) (BT)
- Binney, J. J., Davies, R. L., & Illingworth, G. D. 1990, *ApJ*, 361, 78
- Bishop, J. L. 1987, *ApJ*, 322, 618
- Cretton, N., & van den Bosch, F. C. 1999, *ApJ*, in press (astro-ph/9805324)
- de Bruijne, J. H. J., van der Marel, R. P., & de Zeeuw P. T. 1996, *MNRAS*, 282, 909
- Dehnen, W. D. 1993, *MNRAS*, 265, 250
- Dehnen, W. D. 1995, *MNRAS*, 274, 919
- Dehnen, W. D., & Gerhard, O. E. 1993, *MNRAS*, 261, 311
- Dehnen, W. D., & Gerhard, O. E. 1994, *MNRAS*, 268, 1019
- Dejonghe, H. 1984, *A&A*, 133, 225
- Dejonghe, H. 1986, *Phys. Rep.*, 133, 217
- Dejonghe, H., & de Zeeuw, P. T. 1988, *ApJ*, 333, 90
- de Zeeuw, P.T. 1997, in *The Nature of Elliptical Galaxies*, Proceedings of the Second Stromlo Symposium, eds. Arnaboldi, M., da Costa, G., & Saha, P., p. 44
- Emsellem, E., Monnet, G., & Bacon, R. 1994, *A&A*, 285, 723
- Emsellem, E., Dejonghe, H., & Bacon, R. 1999, *MNRAS*, in press (astro-ph/9810306)
- Evans, N. W. 1993, *MNRAS*, 260, 191
- Evans, N. W. 1994, *MNRAS*, 267, 333
- Evans, N. W., & de Zeeuw, P. T. 1994, *MNRAS*, 271, 202
- Evans, N. W., & Häfner R. M., & de Zeeuw, P. T. 1997, *MNRAS*, 286, 315
- Fehlberg, E. 1968, *NASA Technical Report R-287*
- Franx, M., & Illingworth, G. D. 1988, *ApJ*, 327, L55
- Gerhard, O. E. 1991, *MNRAS*, 250, 812

- Gerhard, O. E., & Binney, J. J. 1996, MNRAS, 279, 993
- Gerhard, O. E., Jeske, G., Saglia, R. P., & Bender, R. 1998, MNRAS, 295, 197
- Hernquist, L., & Ostriker, J. P. 1992, ApJ, 386, 375
- Hunter, C., & de Zeeuw, P. T. 1992, ApJ, 389, 79
- Hunter, C., & Qian, E. E. 1993, MNRAS, 262, 401 (HQ)
- Innanen, K. P., & Papp, K. A. 1977, AJ, 82, 322
- Katz, N., & Richstone, D. O. 1985, ApJ, 296, 331
- Kuijken, K. 1995, ApJ, 446, 194
- Kuijken, K., & Merrifield, M. R. 1993, MNRAS, 264, 712
- Lawson, C. L., & Hanson, R. J. 1974, Solving Least Squares Problems (Englewood Cliffs, New Jersey: Prentice-Hall)
- Lees, J. F., & Schwarzschild, M. 1992, ApJ, 384, 491
- Levison, H. F., & Richstone, D. O. 1985, ApJ, 295, 349
- Levison, H. F., & Richstone, D. O. 1987, ApJ, 314, 476
- Magorrian, J., & Binney J. J. 1994, MNRAS, 271, 949
- Magorrian, J. 1995, MNRAS, 277, 1185
- Matthias, M., & Gerhard, O. E. 1999, MNRAS, submitted (astro-ph/9901036)
- Merritt, D. 1993, ApJ, 413, 79
- Merritt, D. 1996a, ApJ, 486, 102
- Merritt, D. 1996b, AJ, 112, 1085 (M96b)
- Merritt, D., & Fridman, T. 1996, ApJ, 460, 136
- Merritt, D., & Valluri, M. 1996, ApJ, 471, 82
- Morrison, H., Flynn, B., & Freeman, K. C. 1990, AJ, 100,1191
- Ollongren, A. 1962, Bull. Astron. Inst. Neth., 16, 241
- Pfenniger, D. 1984, A&A, 141, 171
- Pfenniger, D., & Friedli D. 1993, A&A, 270, 561
- Press, W. H., Teukolsky, S. A., Vetterling, W. T., & Flannery, B. P. 1992, Numerical Recipes (Cambridge: Cambridge University Press)

- Qian, E. E., de Zeeuw, P. T., van der Marel, R. P., & Hunter, C. 1995, MNRAS, 274, 602 (Q95)
- Richstone, D. O. 1980, ApJ, 238, 103
- Richstone, D. O. 1982, ApJ, 252, 496
- Richstone, D. O. 1984, ApJ, 281, 100
- Richstone, D. O., et al. 1997, in *The Nature of Elliptical Galaxies*, Proceedings of the Second Stromlo Symposium, eds. Arnaboldi, M., da Costa, G., & Saha, P., p. 123
- Richstone, D. O., & Tremaine S. 1984, ApJ, 286, 27
- Richstone, D. O., & Tremaine S. 1985, ApJ, 296, 370
- Richstone, D. O., & Tremaine S. 1988, ApJ, 327, 82
- Rix, H–W., & White, S. D. M. 1992, MNRAS, 254, 389
- Rix, H–W., de Zeeuw, P. T., Cretton N., van der Marel, R. P., & Carollo, C. M. 1997, ApJ, 488, 702 (R97)
- Rybicki, G. B., 1986, in *Structure and Dynamics of Elliptical Galaxies*, ed. P.T. de Zeeuw (Dordrecht: Reidel), p. 397
- Saaf, A. 1968, ApJ, 154, 483
- Schwarzschild, M. 1979, ApJ, 232, 236
- Schwarzschild, M. 1982, ApJ, 263, 599
- Tremaine S., et al. 1994, AJ, 107, 634
- van der Marel, R. P., & Franx, M. 1993, ApJ, 407, 525 (vdMF)
- van der Marel, R. P., de Zeeuw, P. T., Rix, H. W., & Quinlan, G. D. 1997, Nature, 385, 610
- van der Marel, R. P., de Zeeuw, P. T., & Rix, H. W. 1997, ApJ, 488, 119
- van der Marel, R. P., Cretton, N., de Zeeuw, P. T., & Rix, H. W. 1998, ApJ, 493, 613 (vdM98)
- Vandervoort, P. O. 1984, ApJ 287, 475
- Zhao, H. S. 1996a, MNRAS, 278, 488
- Zhao, H. S. 1996b, MNRAS, 283, 149

# EXTENDED SCHWARZSCHILD METHOD

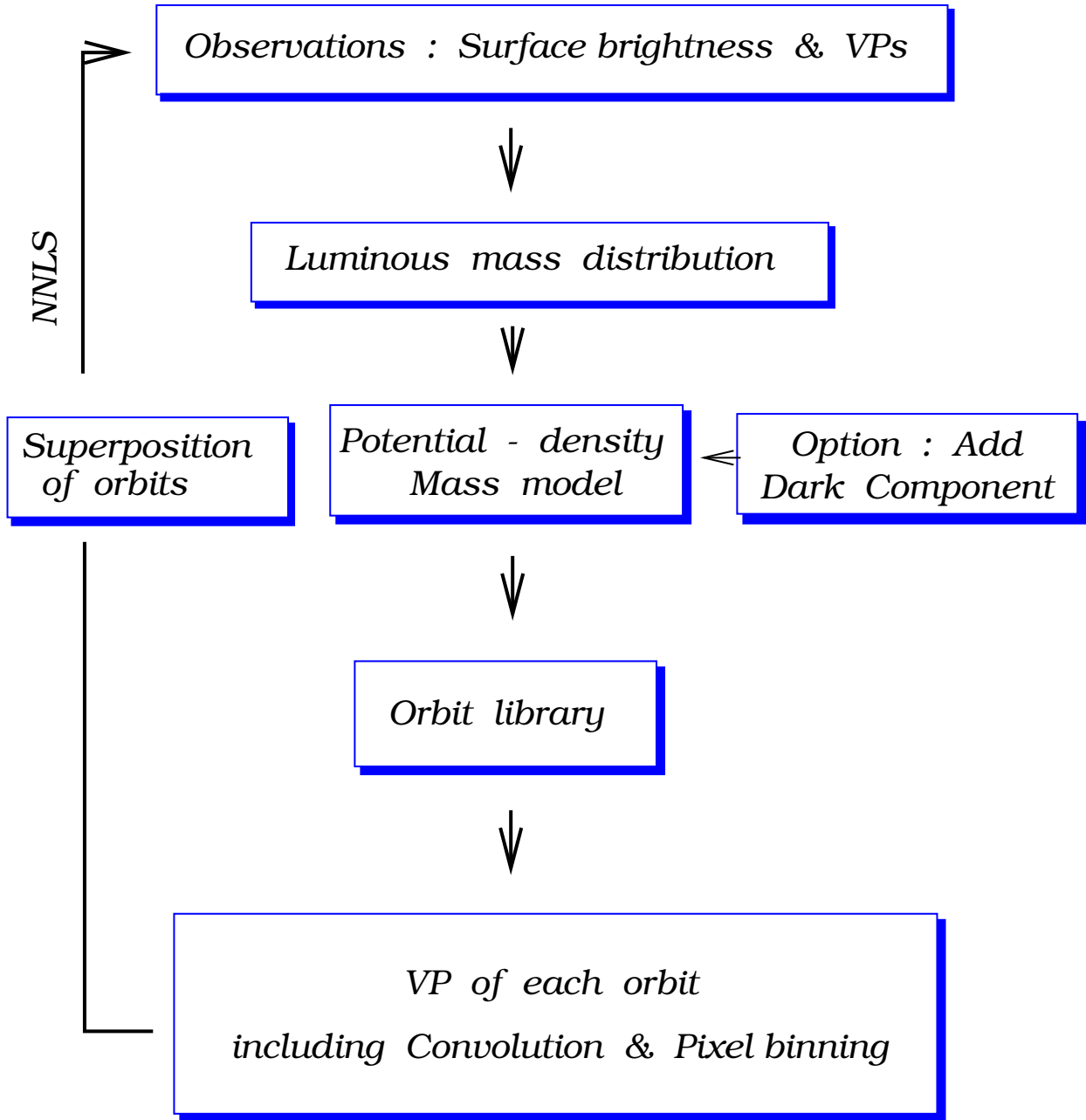


Fig. 1.— Flowchart of the extended Schwarzschild method. We find the non-negative superposition of the orbits with a least squares algorithm (NNLS). This combination of orbits reproduces a set of photometric (surface brightness distribution) and kinematic constraints (VPs).

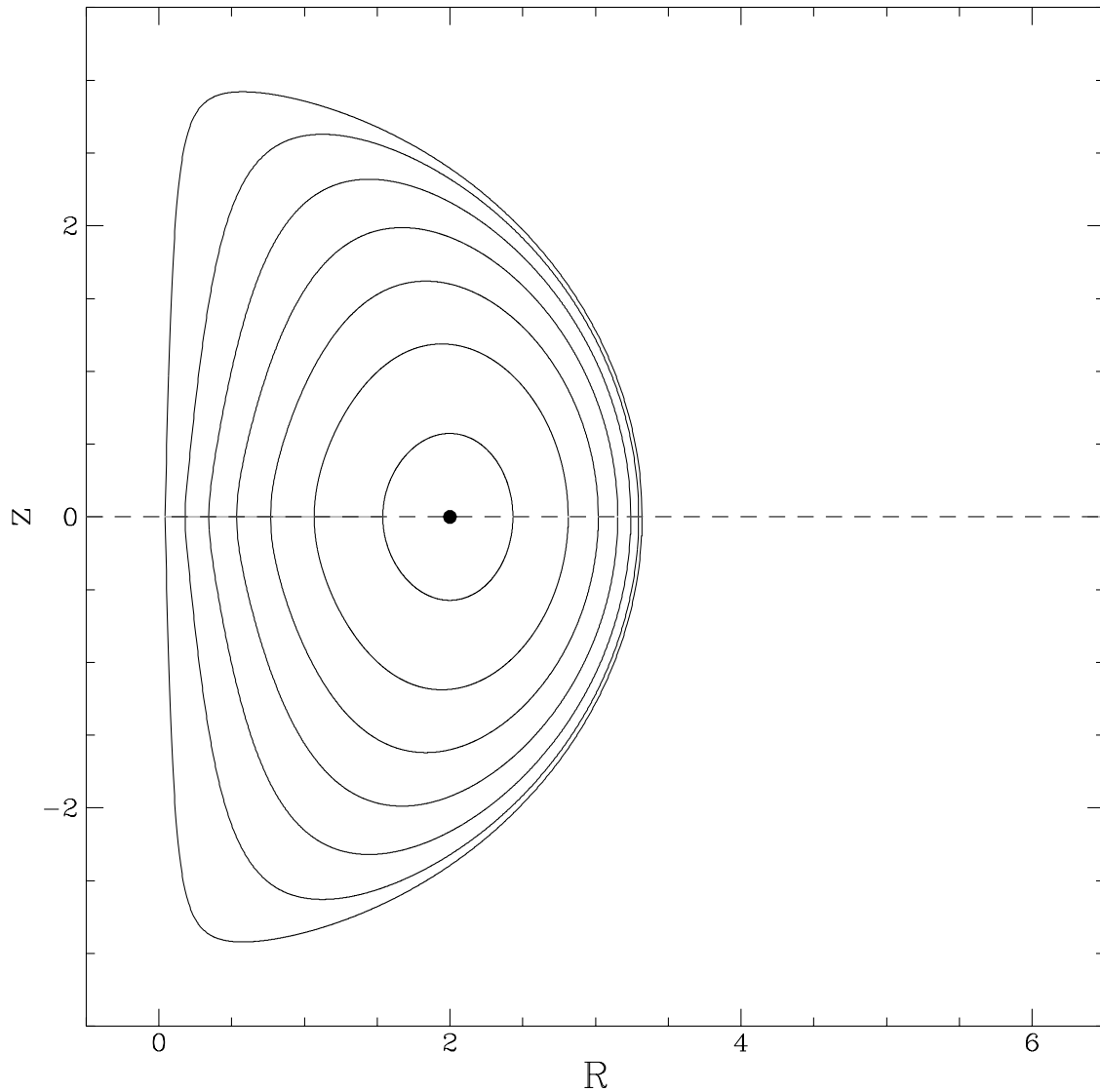


Fig. 2.— Zero Velocity Curves are plotted for 7 values of  $L_z$  uniformly sampled between  $0.05L_z^{\max}$  and  $0.95L_z^{\max}$  at an energy corresponding to a circular orbit radius  $R_c = 2.0$  (indicated by the dot). The mass model is the one of our test model of Section 4.1, with no BH.

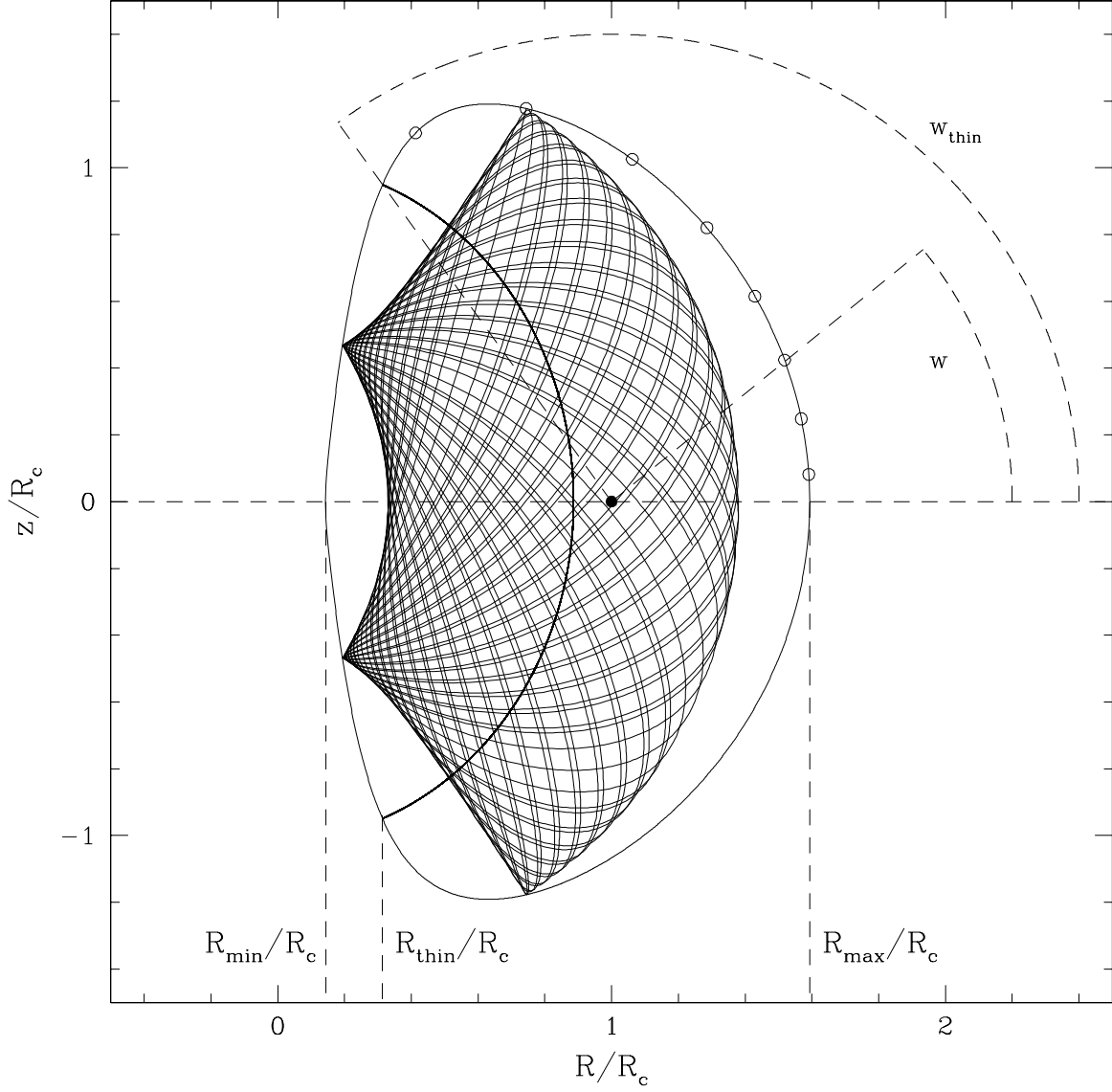


Fig. 3.— A regular orbit, the thin-tube periodic orbit, and the ZVC around them in the meridional  $(R, z)$  plane for the same mass model as in Figure 2. The radii  $R_{\text{min}}$ ,  $R_{\text{max}}$  and  $R_{\text{thin}}$  are indicated (see text). The circular orbit is represented by a black dot. The different starting points on the ZVC are shown with open dots and the corresponding angles  $w$  and  $w_{\text{thin}}$  are indicated.

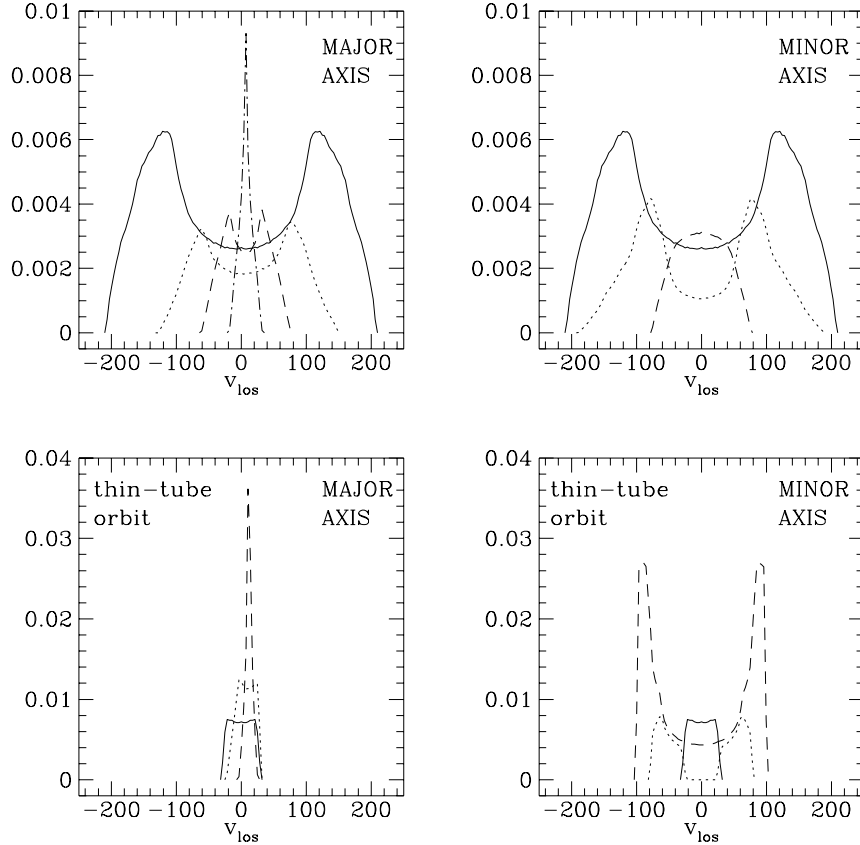


Fig. 4.— VPs as a function of line-of-sight velocity  $v_{\text{los}}$  (in  $\text{km s}^{-1}$ ) for the two orbits of Figure 3. The regular and thin orbits are shown in the top and bottom panels, respectively, for viewing through ( $1''$ -square) cells along the major axis (left) and minor axis (right), respectively. The orbits were not convolved with a PSF. For each panel, different lines correspond to cells at different distances  $r$  from the center: the full line corresponds to the central cell ( $r = 0''$ ), the dotted line to  $r = 1''$ , the short dashed line to  $r = 2''$  and the dot-short dashed line to  $r = 3''$ .

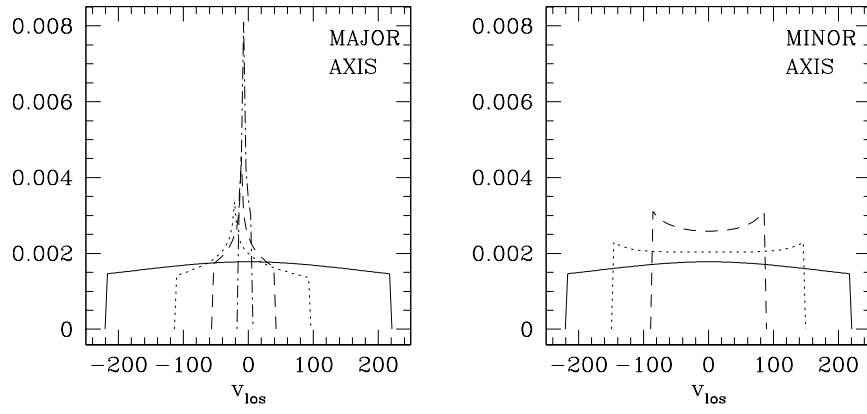


Fig. 5.— VPs of an individual two-integral component with the same  $(E, L_z)$  as the orbits in Figure 3, viewed along the major axis (left) and minor axis (right), respectively. Line types are the same as in Figure 4. However, unlike in Figure 4, these VPs were calculated for a point along either axis, and were not ‘integrated’ over cells.



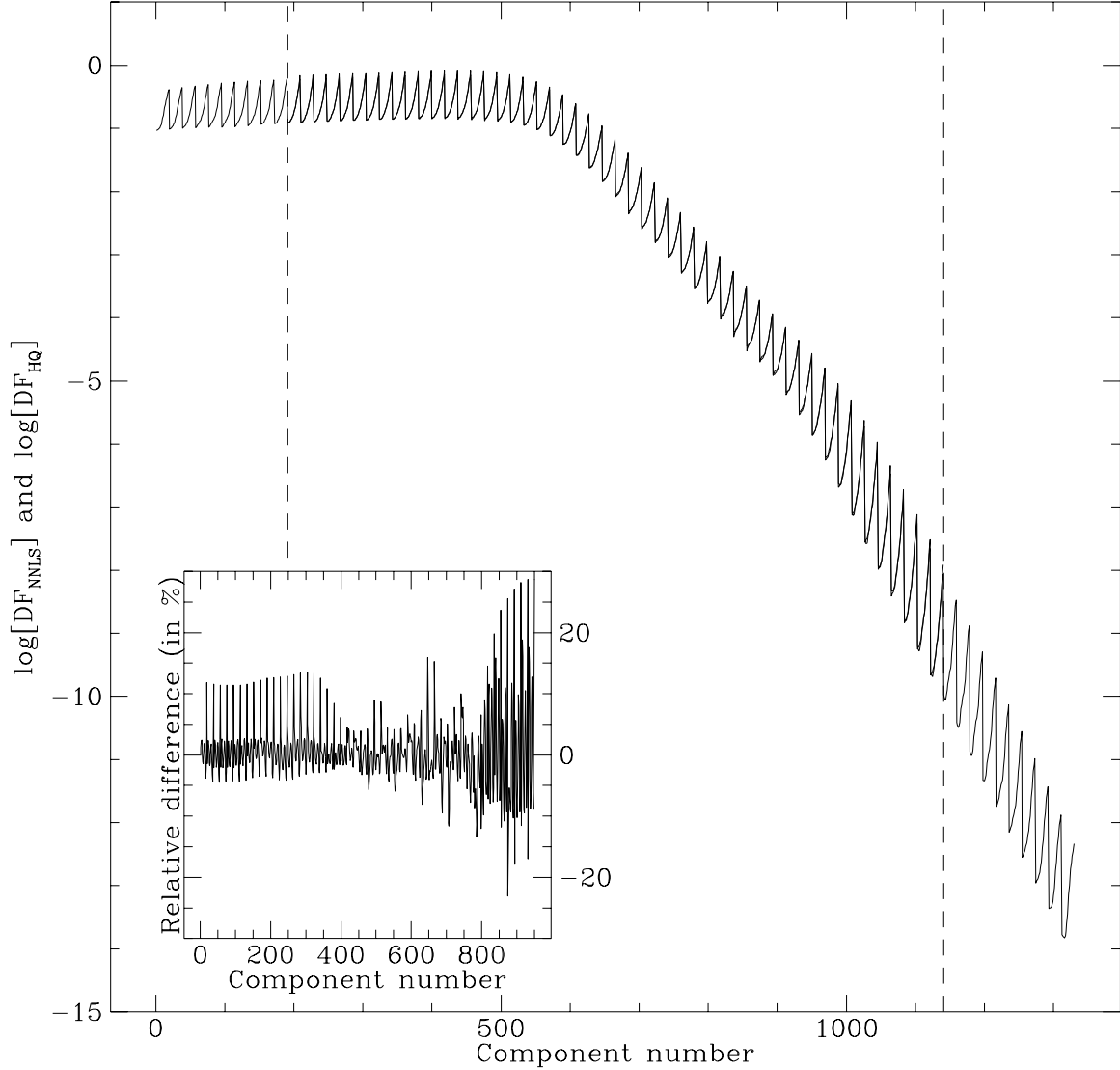


Fig. 6.— The DF  $f(E, L_z)$  for the test model with a  $3 \times 10^6 M_\odot$  BH described in Section 4.1. The DF from the semi-analytical HQ algorithm and from the extended Schwarzschild technique, using only two-integral components, are plotted as function of the component number. The components run in order of energy, and in order of  $L_z$  for each energy; this causes the jagged appearance of the curves. The two curves mostly overlap in the comparison interval (dashed lines). The insert shows the relative difference (in per cent) between the two DFs. The agreement between the two methods of calculating the DF is acceptable.

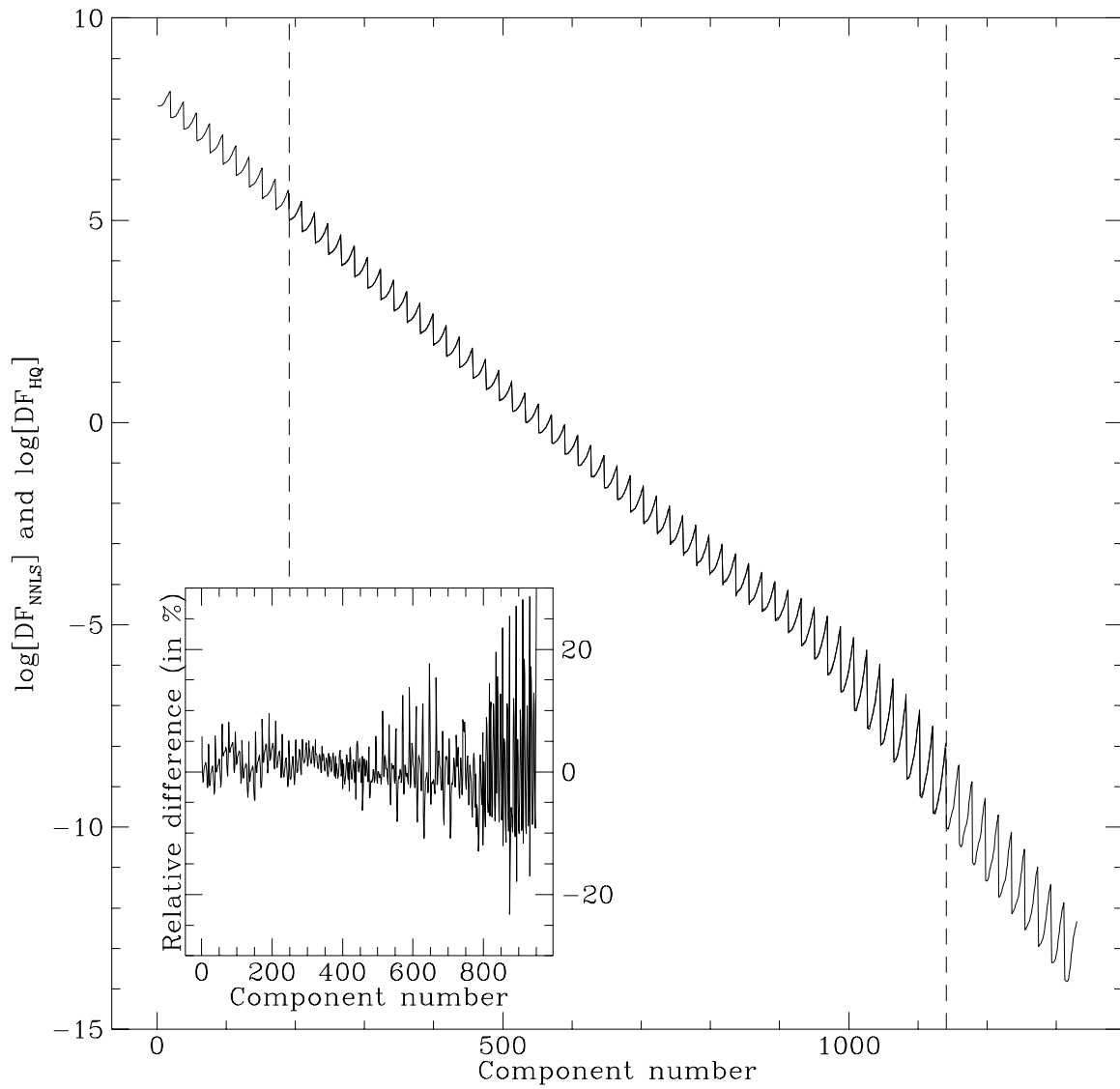


Fig. 7.— Similar to Figure 6, but for the same model without a central BH.

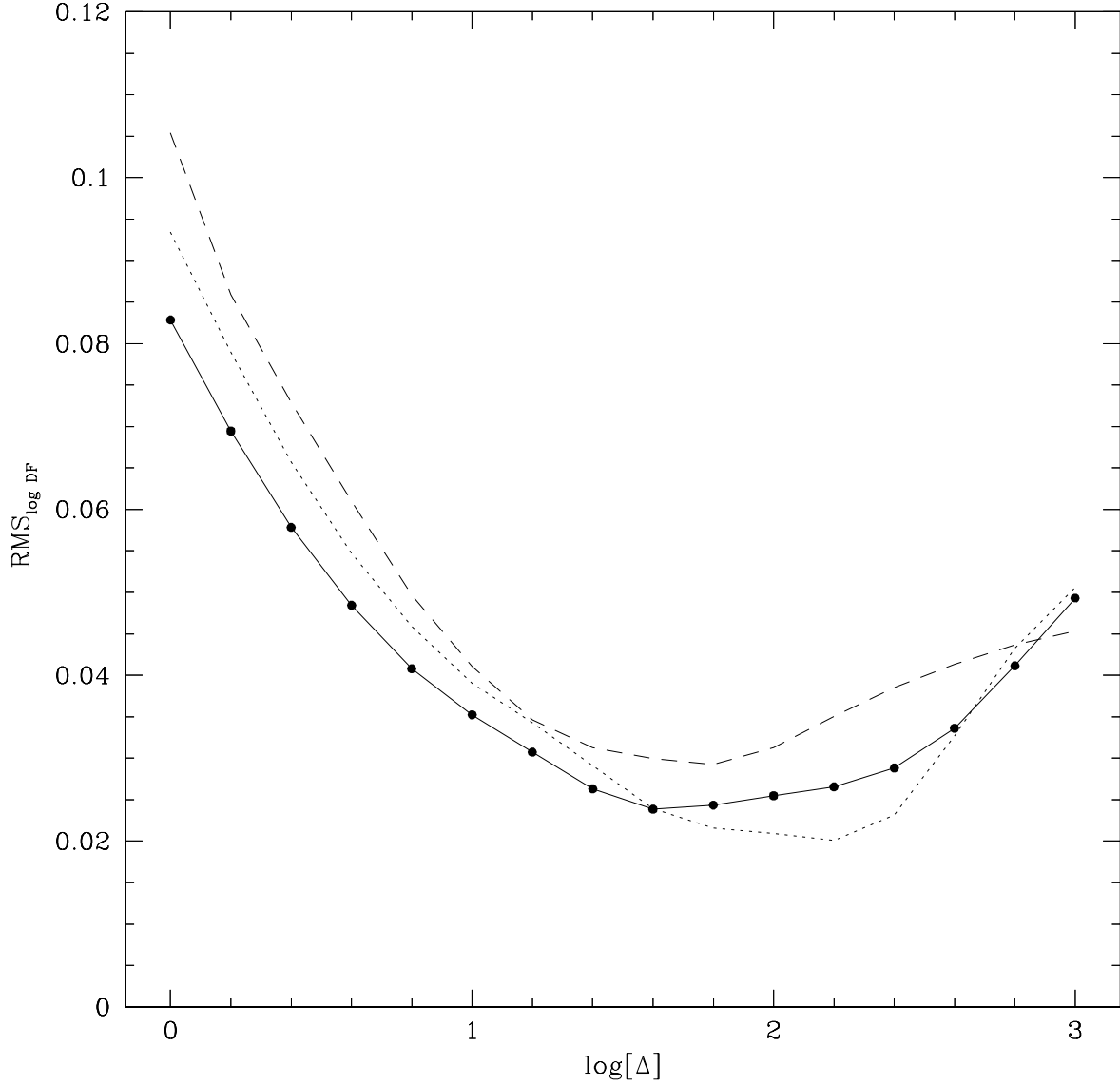


Fig. 8.— The RMS logarithmic residual  $\text{RMS}_{\log \text{DF}}$  for the test model of Figure 7, as function of the logarithm of the regularization parameter  $\Delta$ . The residual measures the difference between the DF as calculated with the semi-analytical HQ algorithm, and as calculated with the extended Schwarzschild technique, using only two-integral components. The different line-types indicate the cases in which only masses in the meridional plane are included as consistency constraints (dotted line), in which only projected plane masses are included (dashed line), or in which both are included (full line with dots).

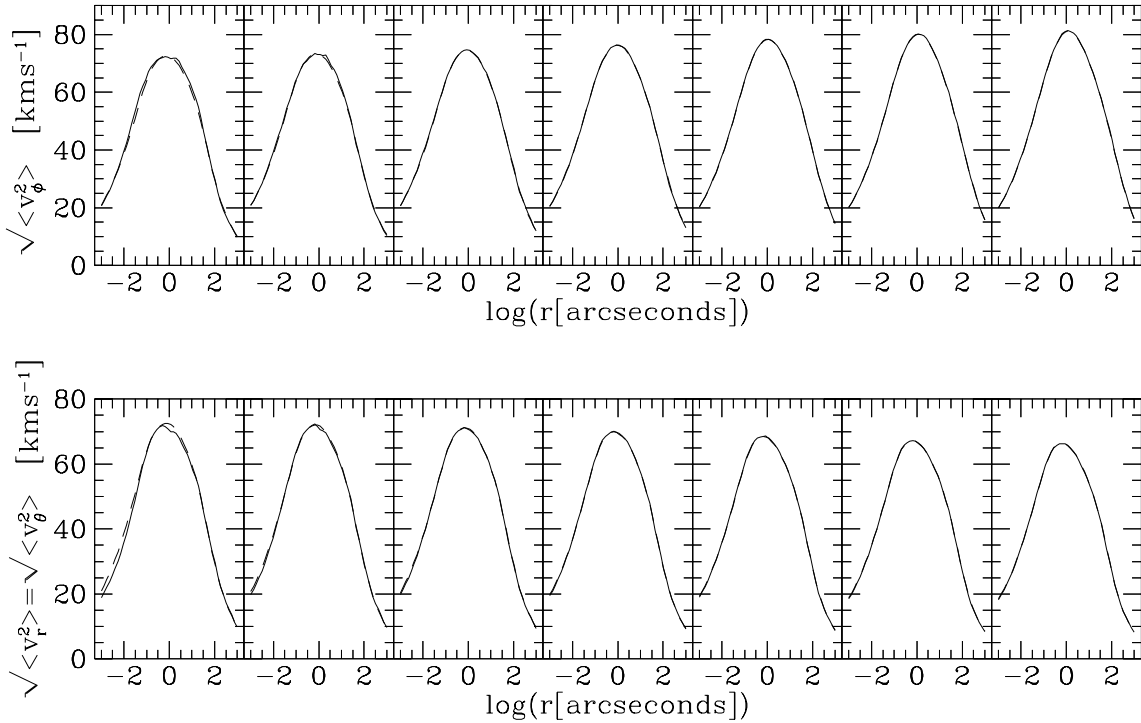


Fig. 9.— Comparison of meridional plane velocity moments, calculated either with the extended Schwarzschild technique using only two-integral components (full curves), or with the Jeans equations (dashed curves), for the model of Figure 7. The top and bottom row of panels show  $\langle v_\phi^2 \rangle^{1/2}$  and  $\langle v_r^2 \rangle^{1/2} = \langle v_\theta^2 \rangle^{1/2}$ , respectively. The meridional  $(r, \theta)$  plane is divided in 7 sectors. In each row, the first panel is the sector closest to the symmetry axis and the last panel is the sector closest to the equatorial plane. The discrepancies are largest near the symmetry axis, but are acceptable everywhere.

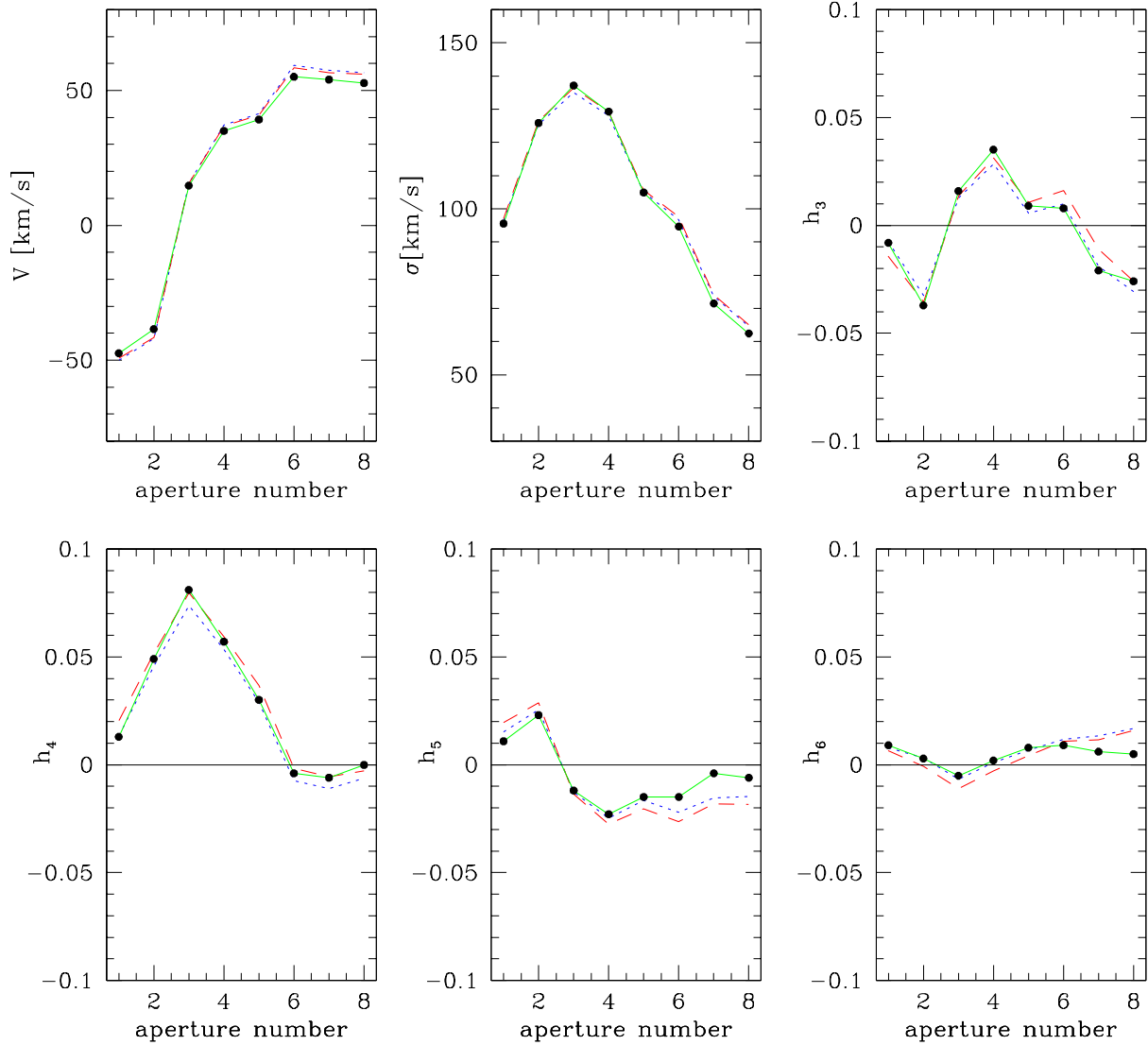


Fig. 10.— Kinematical predictions for the edge-on  $f(E, L_z)$  test model with a  $3 \times 10^6 M_\odot$  BH discussed in Section 4.3. The kinematical apertures are the same as for the HST observations of M32 by van der Marel et al (1997b). They are aligned along the major axis. Data points are plotted equidistantly along the abscissa. Dotted and dashed curves are predictions obtained with the extended Schwarzschild technique, using the software of Cretton and van der Marel, respectively. The solid curves show predictions obtained from direct integration over the DF, using the software of Q95. The three curves agree well, demonstrating the numerical accuracy of the orbit superposition technique.

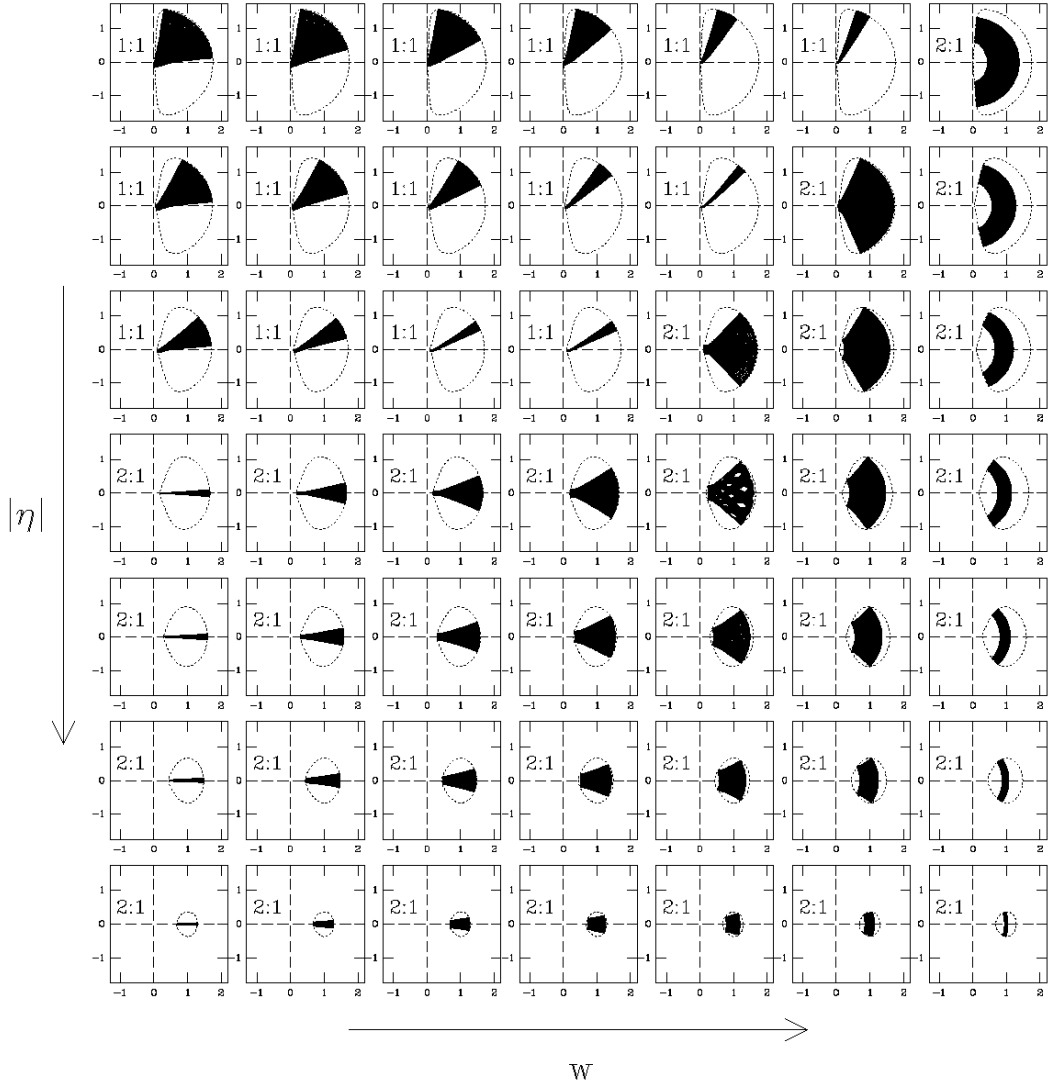


Fig. 11.— Examples of orbits at the energy with  $R_c = 0.25''$ , in the test model of Section 4.1 for the case with a  $3 \times 10^6 M_\odot$  BH. The axes for each orbit are in units of  $R_c$ . Each line corresponds to a different value of  $|\eta|$  and each column to a different value of the third integral. The ratio of the  $R$ - and  $z$ -frequencies for the parent orbit is indicated for those orbits that are not parented by the thin tube.

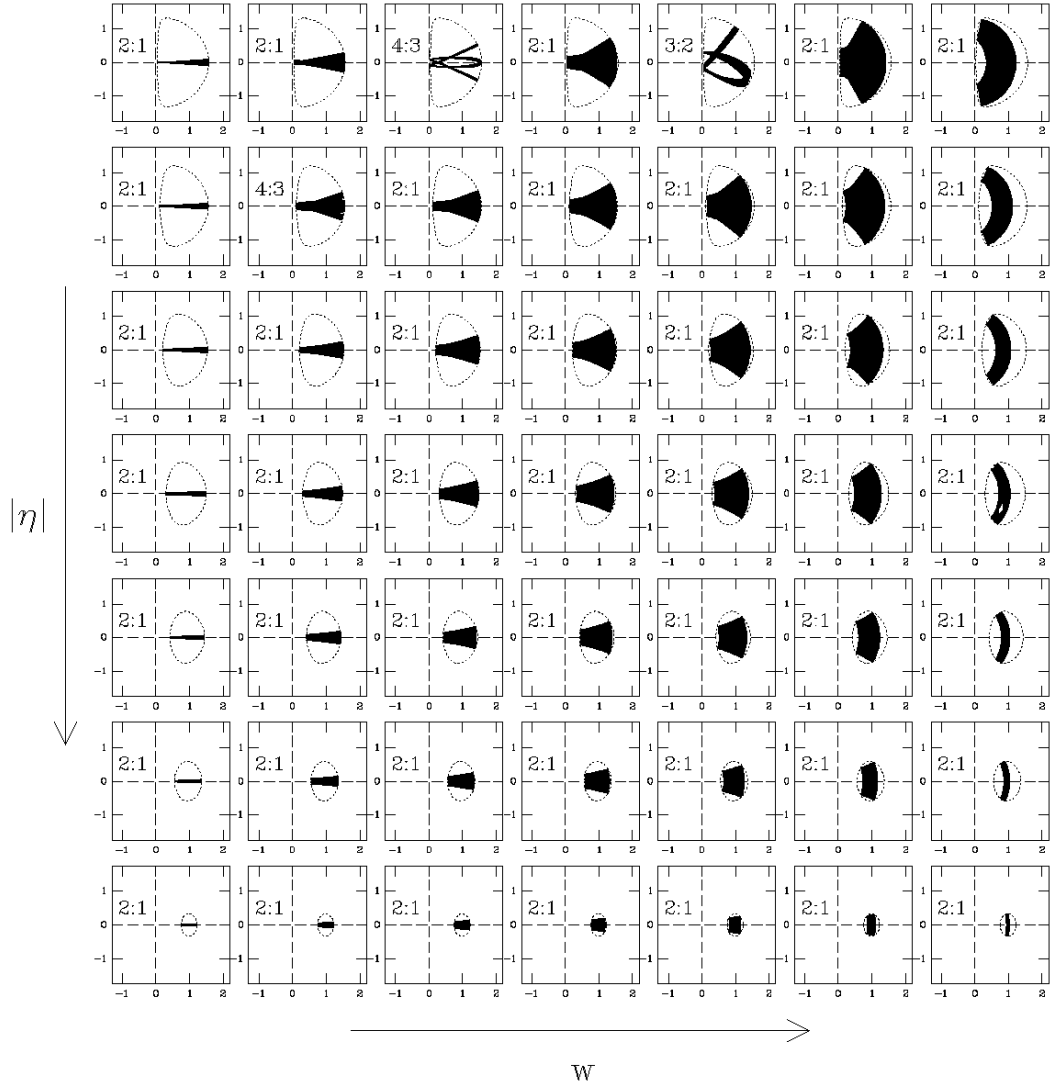


Fig. 12.— Similar as Figure 11, but now for the same model without a central BH.